2013

Nanotube film-enhanced 3-D photoanode for application in microsystems technology

Fareed Dawan
Louisiana State University and Agricultural and Mechanical College

NANOTUBE FILM-ENHANCED 3-D PHOTOANODE FOR APPLICATION IN MICROSYSTEMS TECHNOLOGY

A Dissertation

Submitted to the Graduate Faculty of the
Louisiana State University and
Agricultural and Mechanical College
in partial fulfillment of the
requirements for the degree of
Doctor of Philosophy

in

The Department of Mechanical and Industrial Engineering

by
Fareed Dawan
B.S., Louisiana State University, 2002
M.E., Southern University, 2006
May 2014

This work is dedicated to my wonderful parents James and Deborah, my brother Hashim, and my sister Nisreen.

I also dedicate this work to my son Elias Na'im Dawan and my daughter Evie Inaya Dawan who bring a smile to my face every day.

Thank you.

ACKNOWLEDGEMENTS

I would like to acknowledge my advisor Dr. Eyassu Woldesenbet for providing me unwavering support throughout my entire graduate school tenure.

I would like to thank my graduate committee Dr. Sunggook Park, Dr. Ying Wang, Dr. Zhiqiang Deng for serving as the Dean's Representative, and Dr. Yoonyoung Jin for their expert guidance in my research. Dr. Jin has guided me all the way through, from starting as an REU student, to my Masters, to now. What he has taught me is invaluable. Dr. Jin is a remarkable man, mentor, colleague, and friend. Many have helped me on this journey, which started years before graduate school. To name a few: Dr. John Scott, Ms. Shaloma Malveaux, Dr. Yohannes Desta, Dr. Kun Lian, Dr. Jost Goettert, and Dr. Samuel Ibekwe. Also, I would like to thank Dr. Scott Wicker of the Department of Chemistry at Southern University for his assistance.

I would also like to extend my gratitude to my many colleagues and friends who made this journey enjoyable, including Ms. Lulit Affin, Mr. Emmanuel Gikunoo, Dr. Ali Ghamsari, Dr. Ephraim Zegeye, Mr. Ryan Mallery, and Ms. Jillian Crawley-Foster. A special thank you is deserved to Mr. Niteesh Morampudi, who without his determination and help, this work would still be in progress. I would like to further extend my thanks to Mr. Isaac Stewart, my friend of more than twenty years for at least attempting to keep me focused. Surrounding yourself with those who care and are supportive is essential to success.

This research was supported by the National Science Foundations' Next Generation Composites CREST Center under grant number 0932300.

TABLE OF CONTENTS

LIST OF TABLES

LIST OF FIGURES

ABSTRACT

Surface area plays an important factor in the energy conversion performance of solar cells. It has also emerged as a critical factor in the evolution of high-performance micro-electro-mechanical systems (MEMS) and multifunctional microstructures most of which will benefit from integrated on-chip solar power. Presented here is the hierarchical fabrication and characterization of TiO_2 nanotubes on non-planar 3-dimensional microstructures for enhanced performance of the photoanode in dye-sensitized solar cells (DSSCs). The objective is to increase photoanode performance within a 1 cm^2 lateral footprint area by increasing the vertical surface area through the formation of TiO_2 nanotubes on 3-D microstructures. In the interest of the seamless integration of DSSCs into MEMS applications, bulk micromachining using wet-etching was employed to fabricate 3-D microstructures in silicon. Anodization was used to form titania nanotubes within sputtered titanium thin films. Film quality, adhesion, and the formation of the nanotubes are discussed. Nanotubes with approximate outer diameter dimensions of 180 nm, inner diameter of 75 nm, and heights of 340 nm on 15 um^2 x 15 um-deep micro-wells were fabricated resulting in more than 7 times the increase in surface area over planar surfaces. Grazing incidence diffraction measurements were used to negate the substrate contribution while providing a detailed in-depth profile analysis to validate the preferred polycrystalline rutile and anatase orientation on the 3-D surface-texture photoanode. The increase in surface area resulted in an equal increase in dye adsorption capacity and a 78% reduction in spectral reflectance. The optical enhancement of this hierarchically-structured nanotube film-enhanced (NFE) 3-D photoanode correlated well to a high current density increase 10 times that of its flat counterpart. Fabrication of a DSSC utilizing the NFE 3-D photoanode was also performed and tested for its photocurrent performance under solar simulation. Results suggest that although the surface-

textured anode increases the performance of the photoanode, efficiency of the overall cell significantly depends on the architecture. A conceptual implementation of the NFE 3-D photoanode into microsystems is also discussed along with conclusions and suggestions for future work.

CHAPTER 1. INTRODUCTION

1.1 Demand for Renewable Energy

The rapid depletion of the world's non-renewable fossil fuel energy supply has created an urgent demand for alternative renewable energies. The Energy Information Administration (EIA) as well as the International Energy Agency (IEA) has identified hydroelectricity, wood, wind, solar, geothermal, and biomass as primary renewable energy sources. Currently, renewable energy consumption only amounts to 8% share of the total non-renewable energy consumed [1,2]. Of these alternatives, harvesting solar energy via solar technology has not seen the most growth either commercially or economically (See Figure 1.1). Increasing the market and end-use of solar technology, specifically solar/photovoltaic cells, relies upon continued research and development in this area. Solar energy and technology remain, however, to be a promising alternative primarily due to the source of the solar energy, the Sun. Shown in Figure 1.2 [3], sunlight is a range of energies from wavelengths of 100 nm (ultraviolet) to 1100 nm (infrared). The overall spectral irradiation reduces at sea level due to natural atmospheric filtration by cloud cover, air moisture, etc. Therefore in terms of power, the surface of the Earth on average receives 1000 watts/m^2 daily [4]. In terms of solar to electrical energy conversion efficiency, researchers are challenged to utilize this entire energy spectrum. The environmental impact in the use of solar technology is minimum and is thus considered sustainable, green energy. Expected to remain active for the next 6.5 billion years, the sun is considered a stable energy source. Another advantage of solar technology is that it provides on-the-grid power (for homes, plants, and businesses) as well as off-the-grid energy supply for personal and portable use (cell phones, all-terrain and air vehicles, etc).

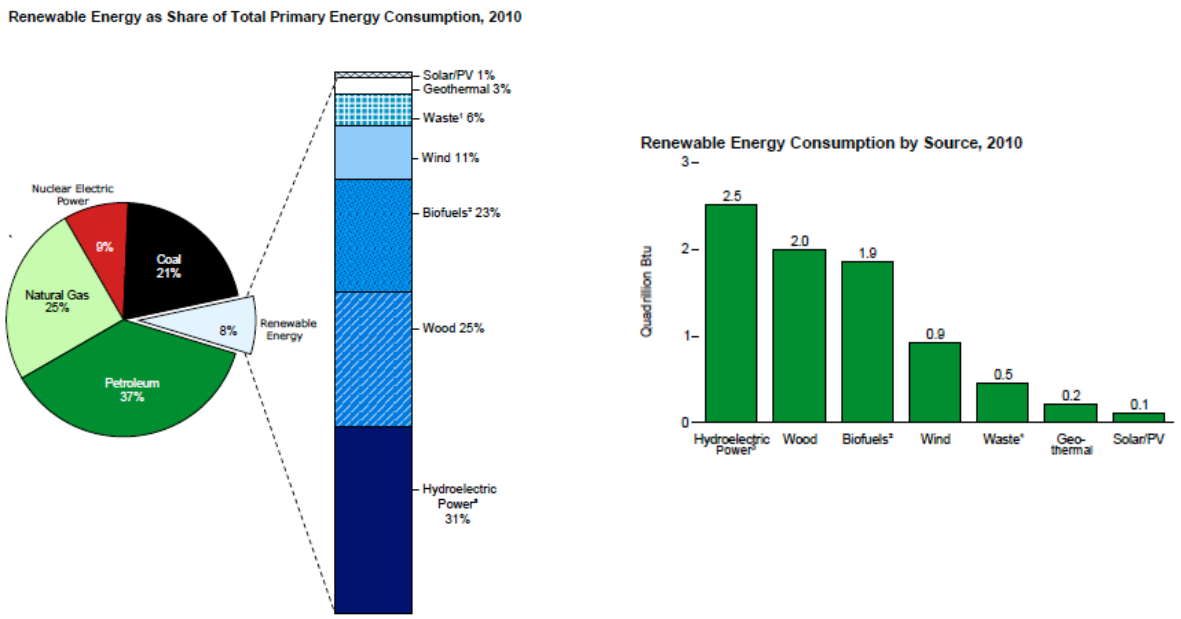

Figure 1.1. Consumption of renewable energy by source and as a share of renewable energy [1,2].

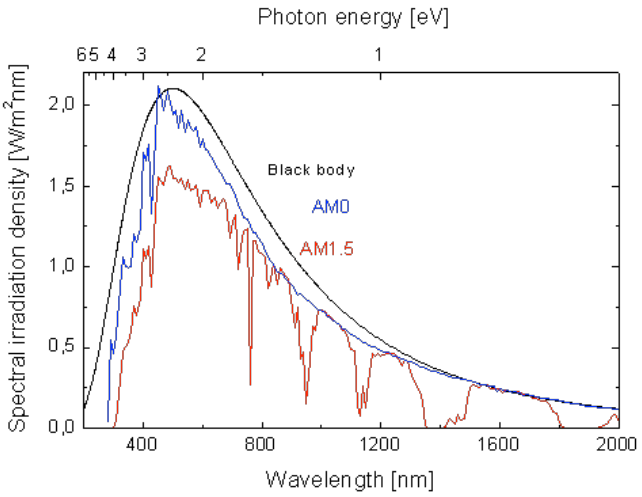

Figure 1.2. Solar energy spectrum at Earth's outer atmosphere (black body), stratosphere (AM0), and sea level (AM1.5) [3].

1.2 Solar Cell Technology

Solar cell technology has been continuously developed since the discovery of the photovoltaic (PV) effect by A. E. Becquerel in 1839. Encyclopedia Britannica Online defines the PV effect as a process in which two dissimilar materials in close contact produce an electrical voltage when struck by light or other radiant energy [5]. This dissimilarity is an electronic

atomic property. From the atomic scale, materials consist of atoms. Electrons orbit the atoms. The number and proximity of these electrons to the core of the atom depend on the element. A pure single element is composed of a periodic arrangement, or crystalline lattice, of an atom. The interaction between 2 or more different elements is an interaction between the electrons in the outer orbital of the atom. The orbitals have energy levels. These energy levels are grouped in bands and are separated by gaps. The gaps are energy levels for which an electron cannot exist.

1.2.1 Energy Band Gap

The energy band gap property of a material defines the amount of energy, measured in electron volts (eV), required to move an electron from the valence band (low energy state) to the conducting band (high energy state). Figure 1.3 is an illustration distinguishing the energy band

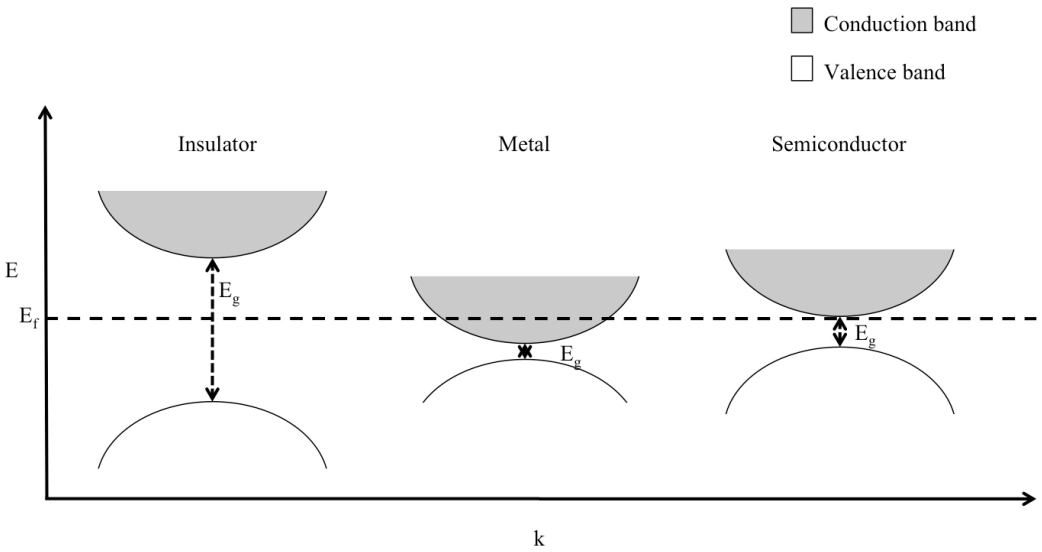

Figure 1.3. Illustration distinguishing the energy band gap (E_g) of an insulator, metal, and a semiconductor.

gap (E_g) of an insulator, metal, and a semiconductor. E_g in an insulator is very large so that electrons cannot be excited into the conduction band. Examples are wood, plastic, and rubber. The E_g in metals is very small with many electrons already present in the conduction band

resulting in material with high electron mobility, or very good conductivity such as silver, copper and gold. Semiconductors have an E_g that falls between an insulator and a conductor. The narrow proximity of the bands means that given an external energy such as heat and/or light, an electron can be excited from the valence band to the conduction band, making many semiconductors ideal PV material. Silicon (Si), with an E_g of 1.1 eV, and Germanium (Ge) with an E_g of 0.7 eV are the most common PV semiconductors. The energy band diagrams for these two are shown in Figure 1.4. In photovoltaic material, incident photon energy equal to the energy band gap is sufficient to excite an electron residing in the valence band (E_v) into the conduction band (E_c). Here, it is important to note that electrons are negatively charged particles (denoted as e^-). When these negatively charged particles are excited into the conduction band, it's positively charged particle counterpart (a hole, denoted as h^+) is left behind and the excited electron is free to move about the atomic lattice. Therefore, the excitation creates what is known as an electron-hole (e^--h^+) pair. Incident photon energy greater or less than E_g will either pass through the material or be absorbed as heat respectively. Si has an indirect band gap, which means that it takes more momentum (k) of the excited electron to be moved into the conduction band, whereas a direct band gap material such as an excited electron in Ge does not require more momentum. In the interest of solar cells, direct E_g material absorbs light more readily than does an indirect E_g material. The Fermi energy level (E_F) defines the probability or potential of an electron being occupied at that energy level. At an equilibrium state, E_F lies within the band gap in insulators, within at least one of the bands in a metal, and near one of the bands in a semiconductor.

Photovoltaics (PVs) are thus semiconducting materials that exhibit this effect and include elements and compounds of Class III – V in the Periodic Table which include various crystalline

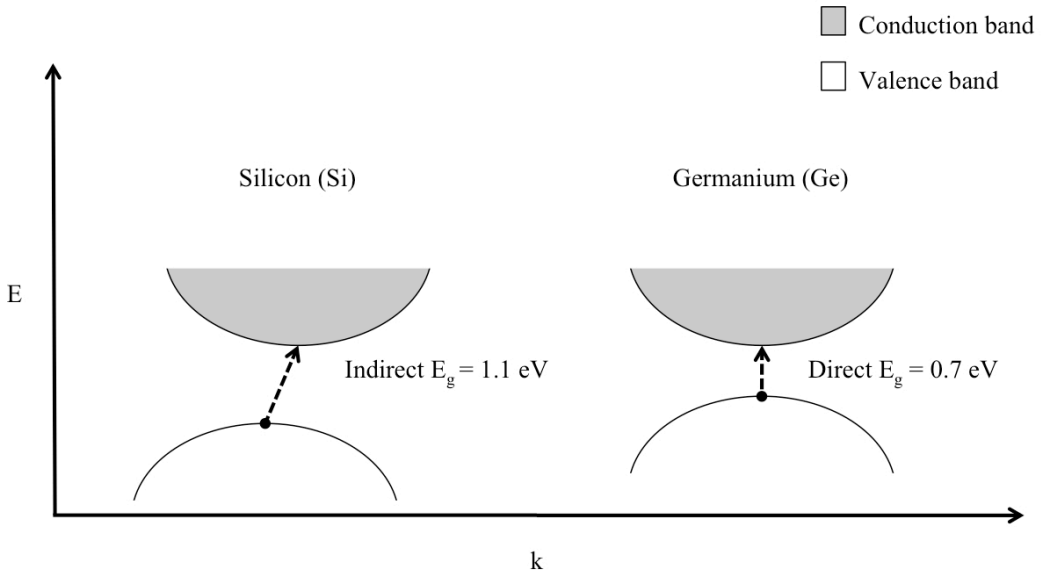

Figure 1.4. Energy band diagrams for Silicon (Si) and Germanium (Ge).

forms of Si and compounds of Cadmium (Cd), Copper (Cu), Telluride (Te), and Selenide (Se). A solar cell is a unit constructed around the PV material to capture and utilize the e-h pair generated from the illuminated PV. Since the conduction of a semiconductor is weak, the excited and mobile electron cannot travel far within the material. Providing a highly conductive medium such as metal for the electron to travel through allows utilization of the mobile electron, or current, to electrically power an external load or device. The first solar cell made by Charles Fritts in 1887 was constructed of Se coated with a thin gold layer [6]. Upon exposure to light, the electrons in the valence band were ejected into the conductance band of the Se (E_g = 1.74). The highly conducting gold metal film coating served as a pathway for these moving electrons to travel through. The efficiency of this and other first solar cells was very low, and so research began to focus on a more light responsive, more efficient material. Modifying the electronic properties of semiconductors via a method called doping can give a semiconductor a more negative charge (n-type) or a more positive charge (p-type) characteristic. Depending on the dopant and its concentration, the E_F level will adjust to be either closer to the minimum of the conduction band meaning that the majority of the charge carriers in the material are electrons (n-

type), or closer to the maximum of the valence band meaning that the majority of the charge carriers in the material are holes (p-type). The illustration for semiconductors in Figure 1.3 depicts an n-type semiconductor. So an n-type semiconductor has electronic properties closer to that of a conductor, whereas a p-type semiconductor's properties are closer to that of an insulator. The dopant for an n-type semiconductor is an atom that would easily give away or donate an outer valence electron such as Phosphorous (P). For a p-type semiconductor an atom that readily accepts electrons such as Boron (B) would be used. Nature says that anything in a high-energy state wants to return to its low-energy state. The same applies for the e-h pair. Current is lost if an excited, high-energy state mobile electron returns to its low-energy state hole counterpart. In addition to this loss, the lifetime of a freed carrier may be short resulting in recombination of an electron-hole pair. The depletion region, near the junction edges within the bulk of the active absorber is where recombination is likely to occur. Recombination is responsible for the largest percentage in efficiency loss in the most advanced solar cell devices. The surface, metal contact areas and defects located within the bulk of the active absorber are the main sources or locations for electron-hole pair recombination. To prevent the recombination of an e-h pair, an energy barrier is introduced. One approach to forming this energy barrier is by joining together p-type and n-type materials. This naturally forms an energy barrier known as a p-n junction. On forming this junction, an internal electric field (E_{int}) at the interface is produced which prevents negative majority charge carriers in the n-type from readily recombining with majority positive charge carriers in the p-type. Figure 1.5 is an example of a p-n junction along with its energy band diagram.

1.2.2 Efficiency and Expense

Evolution of the solar cell is primarily driven by two factors: expense and energy conversion efficiency (ECE). Expense is associated with PV semiconductor material availability and cell processing costs. Si (found extensively in sand) is largely available worldwide and inexpensive ($1.50/lb [7]). Thus, first-generation Si-based solar cells have been widely studied and have seen the most growth and commercial success.

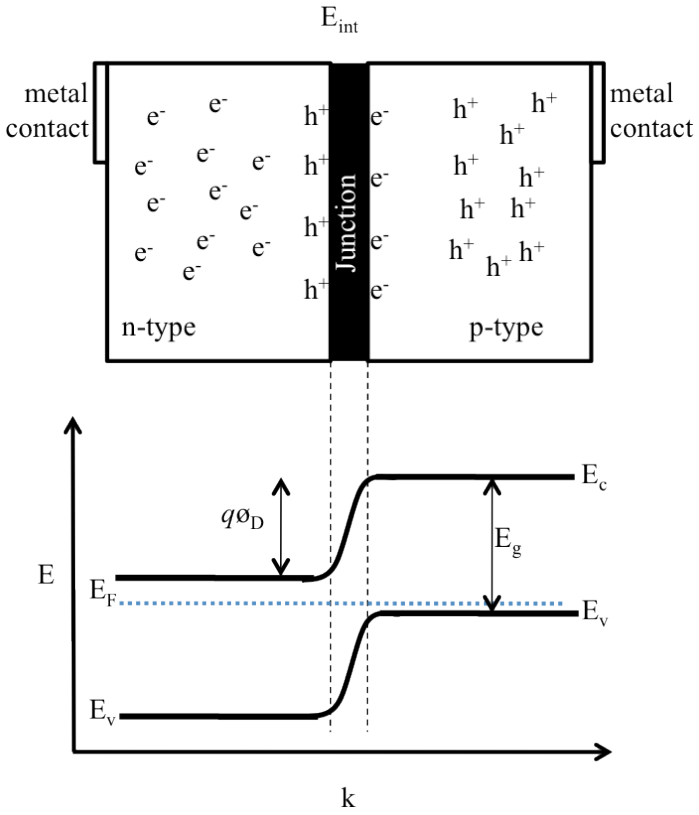

Figure 1.5. Cross-sectional illustration of a p-n junction with its energy band diagram.

Second generation solar cells such as Copper-Indium-Gallium-Selinide (CIGS) cells are the most expensive due to the cost and high toxicity of the material, and difficulty in processing them into thin films. These cells however have attained record-breaking efficiencies but due to their high-cost it is impractical to move them into the commercial mainstream. A basic DSSC usually consists of low-cost materials and is cheaper in processing cost than silicon cells. Table 1.1 lists

the costs in dollars/pound of the most common PV materials. Priced at $4.68/lb, titanium is widely abundant but more expensive than silicon because of the mineral extraction processing required.

Table 1.1. Cost of common photovoltaic material.

PV Material	Cost ($/lb) [7]
Silicon (Si)	1.50
Germanium (Ge)	636
Copper (Cu)	4
Cadmium (Cd)	1.25
Selenide (Se)	65
Titanium (Ti)	4.68
Gallium (Ga)	318
Arsenic (As)	0.70
Indium (In)	309
Platinum (Pt)	116.96
Aluminum (Al)	1.20

Efficiency (n) of a solar cell is defined by the maximum power (P_m) over the product of the incident light intensity (E) and cell surface area (A_c).

$$n = P_m / (E \times A_c) \quad (1)$$

As surface area increases, the amount of dye-coverage area also increases. This results in an increase in the generation of more e-h pairs. Fill Factor (FF) is also important. FF is defined as the ratio of the maximum obtainable power to the product of the open circuit voltage (V_{oc}) and short circuit current (I_{sc}).

$$FF = P_m / V_{oc} \times I_{sc}, \quad (2)$$

Where

$$P_m = n \times A_c \times E. \quad (3)$$

Experimentally, these values can be obtained by measuring the current-voltage characteristics of the PV material. Figure 1.6 is an example of a current-voltage (I-V) curve for a PV semiconductor. When not illuminated, the I-V curve follows a profile shown by the solid line. When illuminated the I-V curve follows a profiles shown by the hashed line. The open circuit voltage is where the curve intercepts the x-axis, and the short-circuit current is where the curve intercepts the y-axis. P_m indicated on the hashed curve is the short-circuit current times the open-circuit voltage. Essentially when there is no light, the solar cell behaves as a diode. The profile of a diode is due the energy barrier created by the joining of two dissimilar metals as discussed in

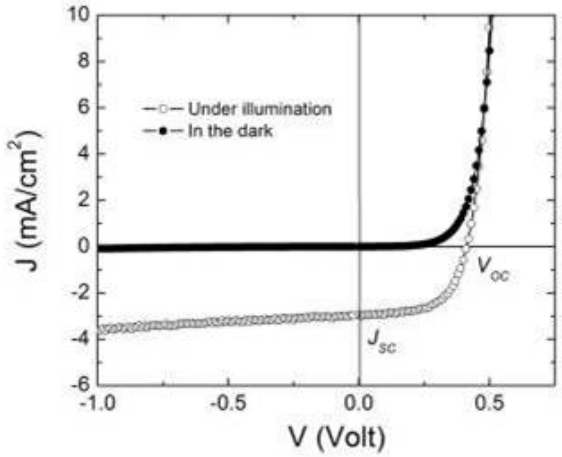

Figure 1.6. Current density versus voltage curve for a solar cell [8].

the previous sections. Since the maximum power is directly related to surface area, any increase in surface area will have a direct increase on the maximum power, which then results in an increase in fill factor. Therefore, an increase in surface area increases overall cell efficiency through an increase in dye-coverage area, fill factor, and maximum power output. Furthermore, the energy conversion efficiency (ECE) is also largely dependent on the electronic properties of the material, specifically the band-gap. Researchers are investing efforts towards altering the

energy band gap of materials. In recent years, even with band-gap alteration, the efficiency of Si-based cells has begun to plateau.

1.2.3 Cell Types and Architecture

Essentially, the miniscule e-h pair generation that occurs on the atomic scale in PV material is amplified in a solar cell to promote the generation of more e-h pairs and the production of more current. Table 1.2 lists the types of solar cells, efficiencies and their generation. A solar cell device is the stacking of different materials each with a specific function. Typically the architecture is flat with a photovoltaic semiconductor sandwiched between two metal contacts. Usually a film or thin glass layer covers the cell protecting it from environmental corrosion. Currently there are three generations of solar cells: (1^{st} generation) single and multi-junction Si, (2^{nd} generation) Cadmium (Cd) and Copper (Cu) -based, and (3^{rd} generation) O'Regan and Graetzal dye-sensitized solar cells (DSSCs) and organic solar cells. DSSCs are among a group of newly emerging solar cells based on titanium (Ti). Ti is not a semiconductor but a transitional metal. Titanium dioxide (TiO_2) however, is an n-type semiconductor and a photocatalyst activated/sensitive under ultraviolet 388 nm wavelength.

Table 1.2 Solar cell types and efficiencies by generation [9].

Generation	Device type	Efficiency	Area (cm^2)	Manufacturer
1^{st}	Single junction Si	9.3	0.25	United Solar
	Multi-junction Si	13	0.25	United Solar
		12.5	922	United Solar
2^{nd}	Cadmium-based	15.8	1.05	USF
	Copper-based	18.8	0.449	NREL
		12.2	3651	Siemens Solar
3^{rd}	DSSCs	7.1	112.3	INAP
	Organic	4.3	0.1	Literature

This means that TiO_2 generates e-h pairs upon 388 nm light exposure. The majority of the energy or efficiency loss is due to the semiconductor absorber layer. In this scheme, the loss in efficiency in this layer alone is over 76 percent. Therefore, it is important that a closer look is

given to the "active" absorber layer. A basic DSSC can be fabricated by anyone with minimum skill, however they are known to have the lowest efficiencies. Thus it is of interest to investigate the DSSC further and improve upon its efficiency.

1.3 Microfabrication Technology

Most of today's electronic devices utilize integrated circuitry (IC). Advances in ICs, or microchips, have been driven by consumer demand for personal, portable, on-the-go devices such as laptops, tablets, cell phones, GPS systems, mp3 players, etc. Scientific research is also benefiting from advances in microchip technology by utilizing disposable lab-on-chips, and biological and chemical microarray field analysis devices. Portable devices offer convenience and are meant to be carried on a regular basis, therefore the IC technology trend is continuously driven towards making these devices smaller, lighter, thinner, faster, and cheaper. Furthermore, nearly all of these devices require electrical energy to power them. As mentioned earlier, solar technology is ideally suited for this type of off-the-grid energy requirement. Most of the IC devices, like solar cells, are made using silicon semiconductor wafers or substrates. This similarity has made it possible for silicon-based solar cells to be seamlessly integrated into the semiconductor-manufacturing scheme and onto the microchip devices such as with some calculators and watches. For process reasons to be discussed, the typical Ti-based DSSC and its design currently does not allow for a seamless integration into the semiconductor-manufacturing process, which is key to mass-producing low-cost solar cells.

Microfabrication is the processing method for miniaturizing IC components. If the IC components are made smaller and smaller, then more and more components can be placed into the same or smaller lateral area, giving a single and smaller portable device more and more functionality or features. Micro-electro-mechanical systems (MEMS) is a sub-area of

microfabrication that focuses on this increased functionality in a smaller area, whereas high-aspect-ratio micro-structure technology (HARMST) is another sub-area that focuses on increasing the vertical surface area of the component while maintaining this reduction of the IC component lateral area [10]. This miniaturization of the IC makes ever-smaller, faster, lighter, and thinner devices possible. Microfabrication uses photolithography, a precise microchip mass-production technique that keeps manufacturing costs, and hence device costs, low. Microfabrication can be divided into two main areas: surface and bulk micromachining. Surface micromachining begins at the surface of the substrate and follows a bottom-up approach in the fabrication of micro-components. In contrast, bulk micromachining starts from the surface and proceeds into the surface of the substrate following a top-down fabrication approach. Photolithography is applied in both of these areas, and uses light and a metal-coated glass stencil to selectively pattern photosensitive polymers (photoresists) that are coated onto the surface of a substrate. The resist can either be a temporary chemical resistive layer for bulk micromachining via substrate etching or can be a final permanent component of the microdevice. Some photoresists such as polymethyl methacrylate (PMMA) and SU-8 are used extensively in MEMSs and HARMSTs as permanent high-surface area microsystem components [11-13]. Other less conventional polymers such as polydimethlysiloxane (PDMS) are increasingly becoming more utilized for microfluidic devices and flexible film applications [14-16].

1.4 Concept and Motivation

There are two sources of motivation: (1) Nature, and (2) High efficiency surface-textured silicon-based solar cells. The sun sufficiently powers all activity on Earth, from creating atmospheric temperature differentials producing wind to seasonal changes and fueling the cycle of life. In many ways, nature has effectively utilized this solar energy to sustain life. One of

these ways is through plants. A plant's leaf essentially is nature's solar cell. As is true with solar cells, depending on the application, or the environment or conditions, the outer appearance, form and shape of the leaf change but its function remains the same: photosynthesis– the process a plant undergoes in converting sunlight into chemical energy. For nearly all of the types of leaves, the core of this efficiency is attributed to the effectiveness of light energy capture facilitated by the photoactive chlorophyll, the thinness, flexibility, shape, and the size or surface area of the leaf. To capture more light in low-lighting conditions (such as if the leaf is located in the center of a tree shaded by other leaves), the leaf will have a larger surface area. Conversely, it will have a smaller surface area if it receives too much light (as with leaves located on the outer crown of a tree). The reported efficiency of a common leaf is about 5.4% [17]. The extremely high multitude of leaves on a single tree of which is connected to billions of other trees through the earth results in enough overall energy conversion efficiency to sustain life on the planet. The tree population and the concentration of chlorophyll present on the Earth is staggering as can be seen in Figure 1.7. Engineers have based the design of the DSSC from the leaf and to date, have achieved overall efficiency as high as 12.3 % [18]. It is the goal of this research to continue to follow nature in looking at trees as 3-D microstructures covered with solar cells. Furthermore, since the 3-D structures will be realized using microfabrication technology, it is natural to address on-chip energy requirements for portable off-the-grid MEMS devices by considering the compatibility of the 3-D photoanode fabrication into the existing infrastructure and process for IC manufacturing. This leads to the second source of motivation: high-efficiency surface-textured silicon solar cells.

One approach to increase the efficiency of silicon-based solar cells utilized a surface-texturing technique. The concept of controlled-surface-texturing is an extension of the process

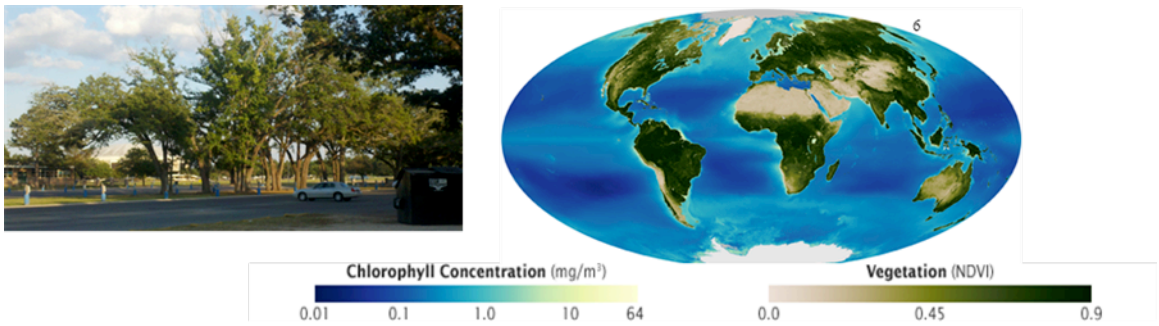

Figure 1.7. Nature's solar cells (leaves) on trees (left). The concentration of chlorophyll on Earth indicating the population of photosynthetic energy generation (right).

reported by Green [19] in the development of the Passivated-Emitter Rear Locally-Diffused (PERL) high efficiency silicon solar cell. The PERL cell utilized inverted pyramidal wells, which effectively increased the absorption of incident light and significantly increased the performance of the silicon solar cell. It was reported that the 3-D textured surface increased the path length of absorbed light resulting in a conversion efficiency of over 23%.

Therefore the concept is, by using high surface area TiO_2-NTs on 3-D surface-textured silicon to further increase the surface area and enhance light retention, we expect to improve the performance of the photoanode and of the typical DSSC. Using microfabrication techniques, this enhanced cost-effective cell could be seamlessly integrated onto microstructures to increase MEMS structures functionality and used to power electrically active MEMS components as illustrated in Figure 1.8.

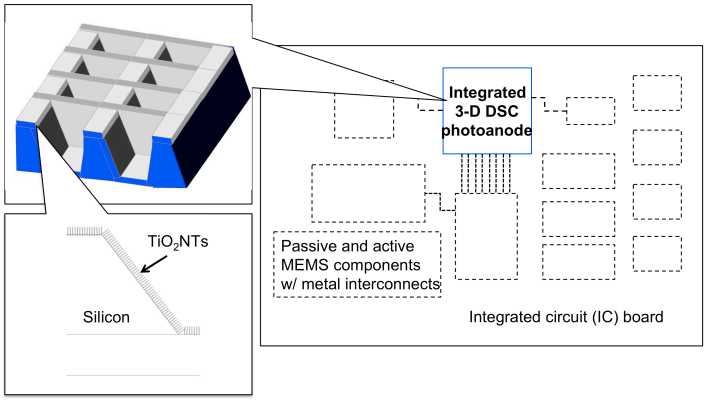

Figure 1.8. Concept of the integration of a hierarchically 3-D structured photoanode into MEMS [20].

1.5 Scope of Work

This research focuses on improving the performance of the titania photo-anode in DSSC. The objective is to increase the performance within a standard 1cm^2 lateral area by increasing the surface area through the formation of TiO_2 nanotubes on 3-D microstructures. In the interest of the integration of DSSCs into MEMS applications, careful attention is given to processing methods of the 3-D surface enhanced photoanode. The structure and content of this report is as follows:

- Chapter 1 provides an introduction into solar cell and microfabrication technology, and gives the concept and motivation behind the research.
- Chapter 2 discusses dye-sensitized solar cells, the mechanisms behind its operation, and the current state-of-the-art.
- Chapter 3 focuses on shape and pattern design consideration for the fabrication of the 3-D surface to maximize surface area. The fabrication approach and method is also discussed.
- Chapter 4 discusses the formation of the titania nanotube film. Consideration of design and affect on surface area is given, followed by a preliminary study on Ti foil and wire format, then the approach and method for nanotube formation in vacuum-assisted Ti thin-film format.
- Chapter 5 is on the characterization of the nanotube film-enhanced 3-D surface. The methods and analysis for the structural phase, optical, and electrical properties are given.
- Chapter 6 is a discussion on the conceptual implementation of the nanotube film-enhanced 3-D photoanode into microsystems.
- Chapter 7 provides a summary of the findings and suggestions for future work.

1.6 References

[1] Annual Energy Review. Accessed on 10/8/12, United States Energy Information Administration, www.eia.gov.

[2] International Energy Agency (IEA), www.iea.org. Accessed on 10/8/12.

[3] Solar spectrum. http://www.superstrate.net/pv/illumination/am.gif. Accessed on 9/20/2012.

[4] The Evolution of Planetary Surfaces, http://www.racetomars.ca/mars/ed-module/planetary_surfaces/index.html. Accessed on 10/19/2012.

[5] Encyclopedia Britannica Online, http://www.britannica.com/EBchecked/topic/458271/photovoltaic-effect. Accessed on 10/19/12.

[6] en.wikipedia.org/wiki/Charles_Fritts, accessed on 12/16/2013.

[7] Mineral Commodities Summary 2012, United States Geological Survey, www.usgs.gov. Accessed on 9/6/12.

[8] Http://photonicswiki.org/images/6/64/Opv_diode_curve.jpg, accessed on 10/15/2013.

[9] R. Bube, Photovoltaic Materials, Properties of Semiconductor Materials-Vol. 1, 2006.

[10] Gad-el-Hak, M. The MEMS Handbook, CRC 2002.

[11] C. Marques, Y. M. Desta, J. Rogers, M. C. Murphy, K. Kelly, Fabrication of High-Aspect-Ratio Microstructures on Planar and Nonplanar Surfaces Using a Modified LIGA Process, Microelectromechanical Systems, 1997, 6, 329-336.

[12] F. Dawan, Y. Jin, J. Goettert, S. Ibekwe, High Functionality of a Polymer Nanocomposite Material for MEMS Applications, Microsystems Technologies, 2008, 14, 1451-1459.

[13] F. B. Dawan, Fabrication and Analysis of a Functional Polymer Nanocomposite for MEMS/HARMS Applications, Southern University, Thesis, 2006.

[14] P. Roca-Cusachs, F. Rico, E. Martinez, J. Toset, R. Farre, D. Navajas, Stability of Microfabricated High Aspect Ratio Structures in Poly(dimethylsiloxane), Langmuir, 2005, 21, 5542-5548.

[15] G. Shao, J. Wu, Z. Cai, W. Wang, Fabrication of Elastomeric High-Aspect Ratio Microstructures Using Polydimethylsiloxane (PDMS) Double Casting Technique, Sensors and Actuators A, 2012, 178, 230-236.

[16] J. J. Boland, Flexible Electronics: Within Touch of Artificial Skin, Nature Materials, 2010, 9, 790-792.

[17] Http://en.wikipedia.org/wiki/Photosynthetic_efficiency. Accessed on 10/20/12.

[18] B. E. Hardin, H. J. Snaith, and M. D. McGehee, The Renaissance of Dye-Sensitized Solar Cells, Nature Photonics, 2012, 6, 162-169.

[19] M. Green, Silicon Solar Cells: Advanced Principles and Practice. Centre for Photovoltaic Devices and Systems, Univ. of New South Wales, Sydney, 1995.

[20] F. Dawan, N. Morampudi, Y. Jin, E. Woldesenbet, Hierarchical Fabrication of TiO_2 Nanotubes on 3-D Microstructures for Enhanced Dye-Sensitized Solar Cell Photoanode for Seamless Microsystems Integration. Journal of Microelectronic Engineering, doi: http://dx.doi.org/10.1016/j.mee.2013.10.007.

CHAPTER 2. DYE-SENSITIZED SOLAR CELLS (DSSC)

2.1 DSSC Design and Mechanisms

The DSSC architecture resembles the cross-sectional view of a leaf. Figure 2.1 illustrates this similarity showing the cross-sectional comparison of a typical DSSC and a leaf. Figure 2.2 is an illustration of the cell's electron generation and transfer process. The functional layers are covered with transparent glass to help protect them against weather/handling damage. Incident sunlight is absorbed by the dye-coated titania photoanode. The photo-conversion process is centered on this layer where electron-hole (e-h) pairs are generated. The photon-excited dye ejects an electron into the titania photoanode. Electrons flow through the photoanode into the adjacent metal contact (anode) where it then flows towards the load, then from the load to the cathode via a conducting pathway. The electrolyte replaces these electrons ejected from the dye and the cathode in-turn replaces this lost electron. This continuous electron transfer and replacement process produces a current flow within the cell. The first DSSCs consisted of a ruthenium complex dye, iodide/triodide electrolyte and a platinum electrode as the cathode. To date, there are several variations to these layer materials briefly listed below:

- Top contact anode material – This anode is ideally transparent as to allow all incident sunlight into the cell. Indium Tin Oxide (ITO), Fluoride Tin Oxide (FTO), and graphene are commonly used for this layer.
- Titania photoanode – The usual DSSC is based on titania, but zinc oxide (ZnO) has also been investigated. This layer can also be used as a top contact anode since the nano-form of titania is transparent, but the conductivity is not as high as ITO, FTO, gold or copper (not transparent). The TiO_2 photoanode is the backbone of the cell. It is usually in a commercially available thin foil format but recent reports have begun investigating vacuum

deposited thin films of titanium. After deposition, the film is modified to make titanium dioxide (titania), which is photocatalytic. The efficiency of this material was of interest after it was discovered that it was able to split water into hydrogen and oxygen [1].

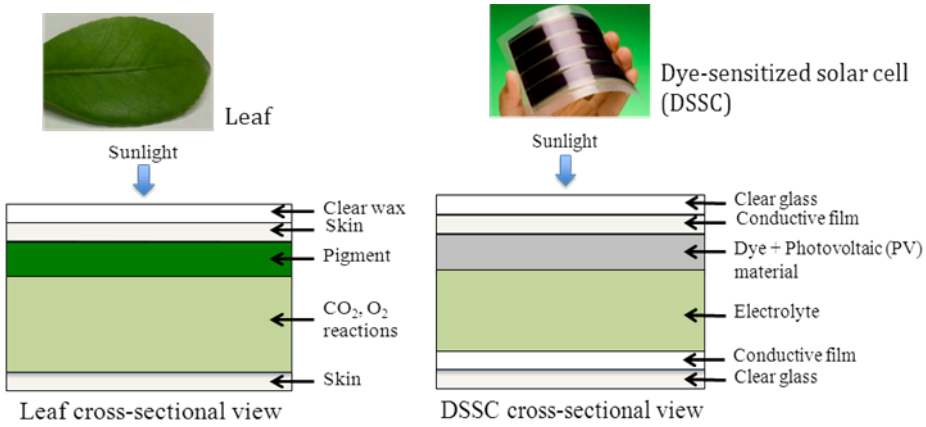

Figure 2.1. Cross-sectional similarities comparing a leaf to a typical DSSC by layer.

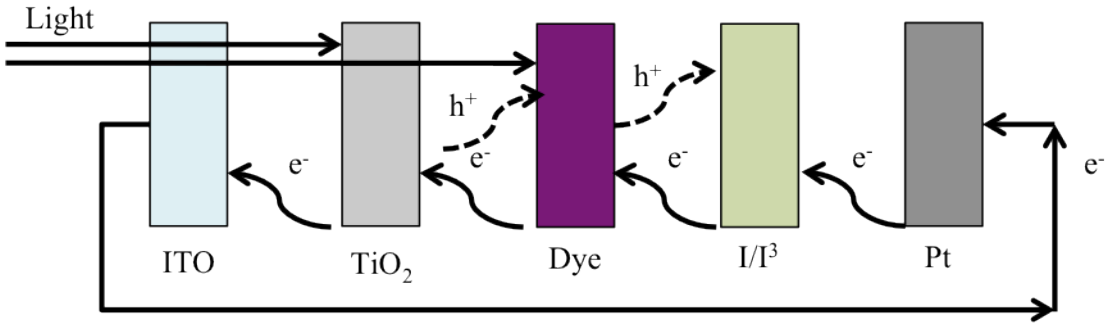

Figure 2.2. An exploded cross-sectional view of the typical DSSC showing the e-h pair generation and transfer mechanism.

The surface and quality of the titania is critical in minimizing e-h pair recombination, increasing e^- transport, and maximizing insolation. Many forms of titania have been investigated from flat films to microparticles, to nanoporous, nanocrystals, to nanotubes where each provides increased surface area respectively.

- Dye sensitizers – The dye enhances the photo absorption wavelength of the UV sensitive only TiO_2. The optimum thickness of this layer on the titania is 20 nm which is sufficient for the ejected electron to avoid recombination and allow transfer from the dye into the titania.

The increase in efficiency for DSSCs is largely attributed to the work in dye synthesis development. Ruthenium complex based dyes including N3, N179, and Black Dye are the most common.

- Electrolytes – There are 5 main types of electrolytes currently being investigated: liquid, ionic liquid, gel, ionic, and solid-state type electrolytes. Liquid-type electrolytes are investigated the most with iodide/triiodide (I^-/I_3^-) as the most efficient. However, the liquid (ionic-type included) form of the electrolyte is a processing disadvantage and also reduces cell lifetime and stability due to leakage concerns. Gel-type electrolytes have the promise of increased stability over liquid-type but at a lower efficiency. Solid-state-type electrolytes are newly being investigated. A recent report has achieved efficiency as high as 10.2 % [2].
- Back contact cathode material – The cathode is usually graphene (C) or platinum (Pt). This is because these two materials are most compatible with the most commonly used liquid-electrolyte iodide/triiodide. The popular carbon allotrope carbon nanotube (CNT) has also shown to be compatible with I^-/I_3^-.

Limiting factors in DSSC efficiency are similar in nature to the 1st and 2nd generation PVs and include e-h pair recombination sites, poor light absorption and trapping, poor electron transfer contact mediums and cell defects in lattice structure.

2.2 DSSC Efficiency

The effect of dye sensitizers and electrolytes on DSSC efficiency has been extensively studied. There is a lack of data on the variations of the photoanode surface area and its effect on efficiency. In fact, many papers fail to mention the surface area of the cell when efficiency values are reported. The graph in Figure 2.3 is a 10-year consolidation of efficiency values reported in literature based on advancements in dye-sensitizers and electrolytes. When these

values are viewed from the photoanode type, such as mesoporous (1), nanoporous (2), nanoparticles (3), and nanocrystals (4), nanotubes (5), nanocolloids (6) the impact of surface area on efficiency can be seen as shown in Figure 2.4. The energy band diagram for the DSSC sheds light on its efficiency. Figure 2.5 is the energy band diagram for a DSSC utilizing FTO as the front and back contacts.

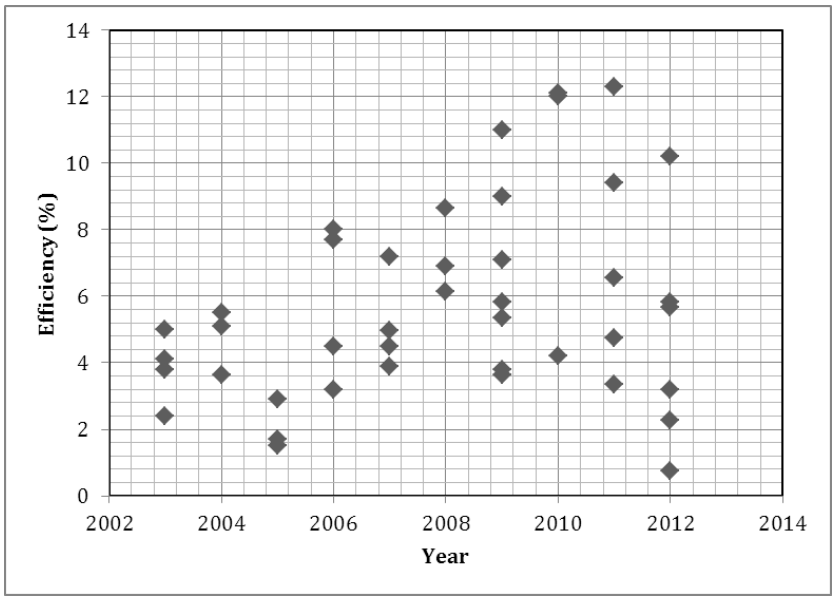

Figure 2.3. Literature reported DSSC efficiencies from 2003 to 2012 [8-11].

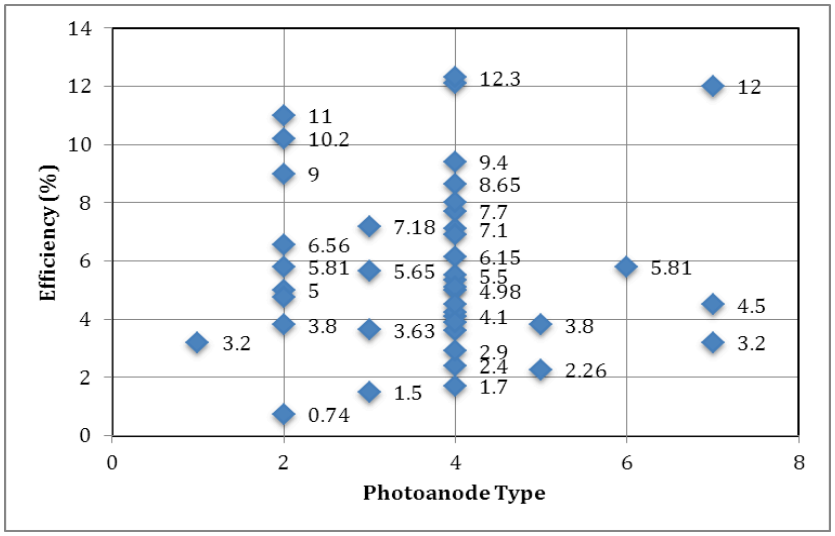

Figure 2.4. Literature reported DSSC efficiency versus the photoanode type. 1: mesoporous, 2:nanoporous, 3:nanoparticles, 4:nanocrystals, 5:nanotubes, 6 nanocolloids, 7:not reported.

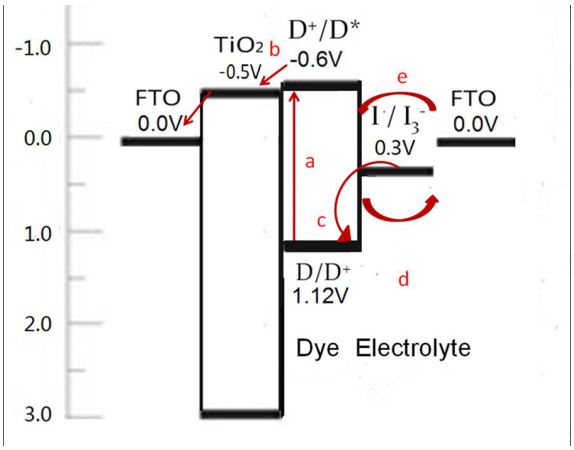

Figure 2.5. The energy band diagram for a DSSC with FTO used as the front and back contacts [4].

2.3 Current State-of-the-Art

As mentioned in Section 2.1, the cross-sectional architecture of the DSSC is similar to that of a leaf. The dye-sensitizer is analogous to the chlorophyll, and the structure and surface area coated by the chlorophyll is analogous to the photoanode coated with the dye. Increasing the photoanode surface area increases the cell surface insolation and dye coverage area, and hence, the multitude of e-h pair generation [3]. An advantage of TiO_2 is its various allotropes. As noted in Section 2.2 and in Figure 2.4, TiO_2 photoanodes have been formed as microparticles, nanoparticles, nanoporous, nanocolloids, mesoporous, nanocrystals, and most recently as nanotubes. Figure 2.6 shows some of them. Of these, the nanotubular form has the most surface area. Furthermore, the nanotubes have been shown to be crystalline in structure and preferentially ordered perpendicular to the surface. This ordered crystalline structure provides a clear pathway of the electron charge to travel or be transferred into the contacting conductive anode [5]. In comparison, microparticles, nanoparticles, and nanocrystals have a high surface area also but their disordered layout results in an increase potential of e-h pair recombination sites reducing the efficiency [6]. Another advantage of the nano-scaled form of TiO_2 is its

apparent transparency to visible light. This property works in favor of DSSCs when considering TiO_2 as a top contact anode.

3-D formats to enhance cell conversion efficiency have been considered. Yiu et al reported on DNA-shaped TiO_2 photoanodes constructed from titanium wire [7].

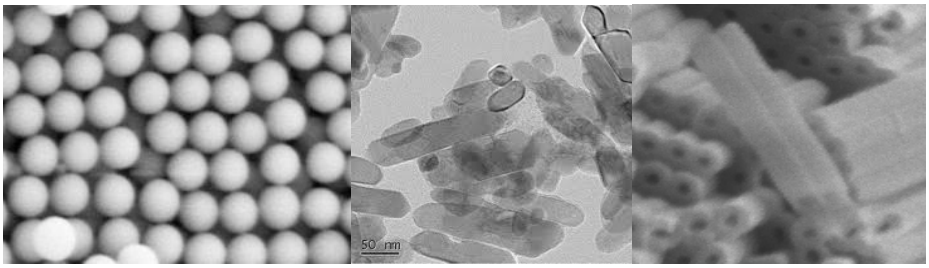

Figure 2.6. Various allotropes of titania. Shown from left to right: microparticles [12], nanocrystals [13], and nanotubes (image taken in our lab).

Nanotubes were grown along the wires surface using anodization. After constructing several of these photoanodes and wiring them together in series and in parallel they achieved a maximum power of 0.49 mW. This maximum power is owed to the wire diameter of 0.4 mm and length of 1.5 cm. This format however poses difficulty for mass production and result consistency, and is challenging to integrate into MEMS.

One aim of this project is to utilize microfabrication processing techniques to fabricate the 3-D structured photoanode cells. This approach will minimize cost and allow mass production of devices with a high yield rate. Since we are extending into the vertical plane using 3-D microstructures and not expanding the lateral plane, it will also address the up-scaling issue encountered with large DSSC formats [14].

Ko et al recently reported on a ZnO nanowire forest for enhanced DSSC efficiency [15]. When compared to single branch ZnO structures, the high-surface area forest configuration had an efficiency 5 times greater. The reported efficiency was 2.63%. Although microfabrication

techniques were used, the hydrothermal fabrication approach requires high-temperatures and chemically aggressive etching which is incompatible with considering a flexible polymer DSSC.

High surface area 3-D photoanodes have also been investigated using 2nd generation materials. Fan et al provides a review and discusses the nanostructuring of Si, CdS, CdSe, CdTe, ZnO, $CuInSe_2$ for use in photovoltaics [16]. The report states that surface area alone does not increase efficiency but that the shape of the nanostructures matters on the effectiveness of light-trapping and charge carrier collection. Though the toxicity and expense of the materials investigated also steer away from the low-cost, flexible advantage of DSSCs.

2.4 References

[1] A. Fujishima, T. N. Rao, D. A. Tryk, Titanium Dioxide Photocatalysis, Journal of Photochemistry and Photobiology C: Photochemistry Reviews, 2000, 1, 1-21.

[2] I. Chung, B. Lee, J. He, R. P. H. Chang, M. G. Kanatzidis, All-Solid-State Dye-Sensitized Solar Cells With High Efficiency, Nature Letter, 2012, 485, 486-490.

[3] R. Yu, Q. Lin, S-F. Leung, Z. Fan, Nanomaterials and nanostructures for efficient light absorption and photovoltaics, Nano Energy 2012, 1, 57-72.

[4] L. Deng, Dye-Sensitized Solar Cells With a Solid Hole Conductor, McMaster University, Thesis, 2012.

[5] G. K. Mor, O. K. Varghese, M. Paulose, K. Shankar, C. A. Grimes, A review on highly ordered, vertically oriented TiO_2 nanotube arrays: Fabrication, material properties, and solar energy applications, Solar Energy Materials & Solar Cells, 2006, 90, 2011–2075.

[6] L. M. Peter, The Gratzel Cell: Where Next?, J. Phys. Chem. Lett. 2011, 2, 1861 – 1867.

[7] Y. Wanga, Y. Liu, H. Yang, H. Wang, H. Shen, M. Li, J. Yan, An investigation of DNA-like structured dye-sensitized solar cells, Current Applied Physics 10, 2010, 119–123.

[8] C-W. Lee, H-P. Lu, C-M. Lan, Y-L. Huang, Y-R. Liang, W-N. Yen, Y-C. Liu, Y-S. Lin, E. W-G. Diau, and C-Y. Yeh, Novel Zinc Porphyrin Sensitizers for Dye-Sensitized Solar Cells: Synthesis and Spectral, Electrochemical, and Photovoltaic Properties, Chem. Eur. J. 2009, 15, 1403 – 1412.

[9] N. F. Atta, H. M.A. Amin, M. W. Khalil, A. Galal, Nanotube Arrays as Photoanodes for Dye Sensitized Solar Cells Using Metal Phthalocyanine Dyes, Int. J. Electrochem. Sci., 2011, 6, 3316 – 3332.

[10] A. Mishra, M. K. R. Fischer, P. Bauerle, Metal-Free Organic Dyes for Dye-Sensitized Solar Cells: From Structure: Property Relationships to Design Rules, Angew. Chem. Int. Ed. 2009, 48, 2474 – 2499.

[11] P. Roy, D. Kim, I. Paramasivam, P. Schmuki, Improved Efficiency of TiO_2 Nanotubes in Dye Sensitized Solar Cells by Decoration With TiO_2 Nanoparticles, Electrochemistry Communications, 2009, 11, 1001–1004.

[12] www.microspheres-nanospheres.com. Accessed on 6/3/12.

[13] www.nanowerk.com. Accessed on 6/3/12.

[14] A. Hagfeldt, G. Boschloo, L. Sun, L. Kloo, and H. Pettersson, Dye-Sensitized Solar Cells, Chem. Rev. 2010, 110, 6595–6663.

[15] S. H. Ko, D. Lee, H. W. Kang, K. H. Nam, J. Y. Yeo, S. J. Hong, C. P. Grigoropoulos, and H. J. Sung, Nanoforest of Hydrothermally Grown Hierarchical ZnO Nanowires for a High Efficiency Dye-Sensitized Solar Cell, Nano Lett. 2011, 11, 666–671.

[16] R. Yu, Q. Lin, S-F. Leung, Z. Fan, Nanomaterials and Nanostructures for Efficient Light Absorption and Photovoltaics, Nano Energy 2012, 1, 57-72.

CHAPTER 3. FABRICATION OF SI-ETCHED 3-D MICROSTRUCTURES

3.1 Introduction

3-dimensional surfaces can be described as any lateral surface that extends into the vertical plane. The technology trend for the solar market as well as microchips is going towards smaller, increased performance, and cheaper devices. Vertical surface area extension is preferred over lateral area expansion to save on the expense of module space allocation or chip board/land real estate. There is an advantage to be able to fit more devices or activity in less lateral area. HARMST is based on this. Nanotechnology is also based on utilization of increased surface area to provide increased sensitivity or reactivity. Materials used in this extension may vary from metallic, composites, or polymers.

3.1.1 Design Considerations

Optimal determination of 3-dimensional microstructures depends on maximal surface area, material, favorable light-structure interaction, and fabrication feasibility. The art of photolithography allows various shapes to be formed in the lateral dimension however focus will be on the squares, circles, and concentric circles shapes. Three dimensionally, these shapes will translate into rectangular columns, cylindrical posts, and cylindrical tubes respectively, when fabricating directly with a photo-sensitive polymer. Figure 3.1 and Figure 3.2 show the difference in surface area for 2-D and 3-D.

The shapes selected for investigation must be feasible to fabricate utilizing cost-effective UV photolithography and microfabrication. This method allows the mass production of array elements of a given shape at one time. Figure 3.3 illustrates the increase in surface area from 1 cm^2 using a 3-D microarray surface. Surface area 4 (SA 4) with titania nanotubes has the highest surface area.

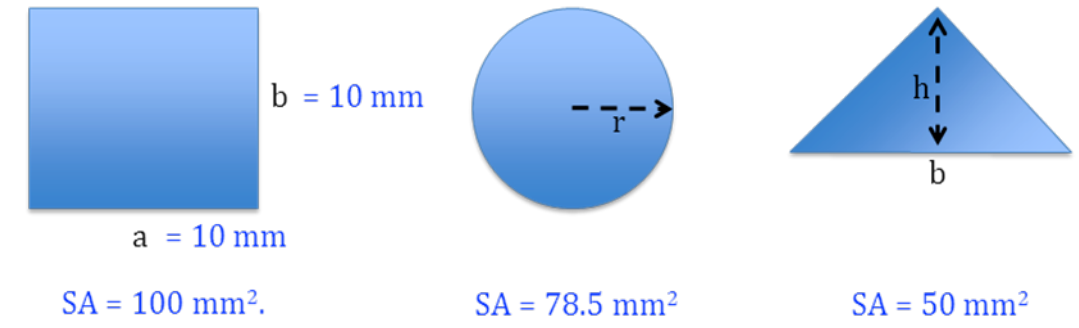

Figure 3.1. Example of surface area for 2-D shapes.

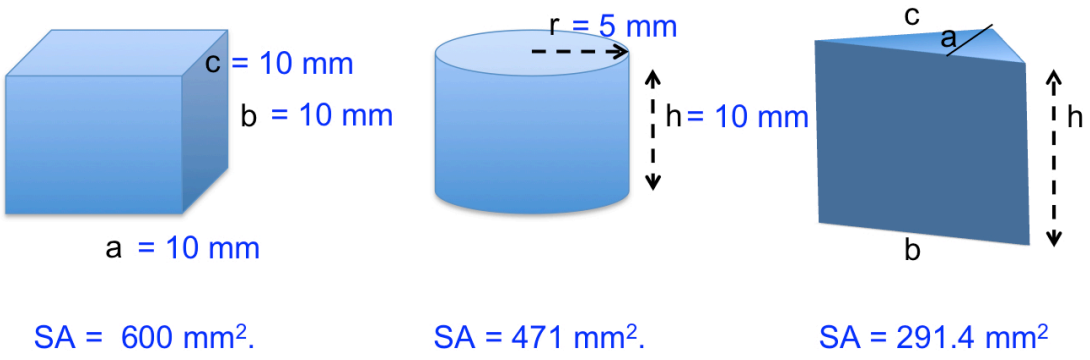

Figure 3.2. Example of surface area for 3-D shapes.

The 3-D shapes considered are the cuboid, the cylinder, the trapezoid, and the triangular prism. Using a 20 µm-square area with only 20 µm height, it can be seen in Figure 3.4 that the cuboid has the highest surface area, followed by the cylinder then the trapezoid. Considering a microarray of these 3 given the same moderate lateral and height dimensions as above, the 1 cm^2 planar surface area is increased to 1.25, 1.17, and 1.10 cm^2 for the cuboid, the cylinder, and the trapezoid, respectively, as illustrated in Figure 3.5.

3.2 Experiment

Microfabrication uses photolithography, a precise microchip mass-production technique that keeps manufacturing costs, and hence device costs, low. Microfabrication can be divided

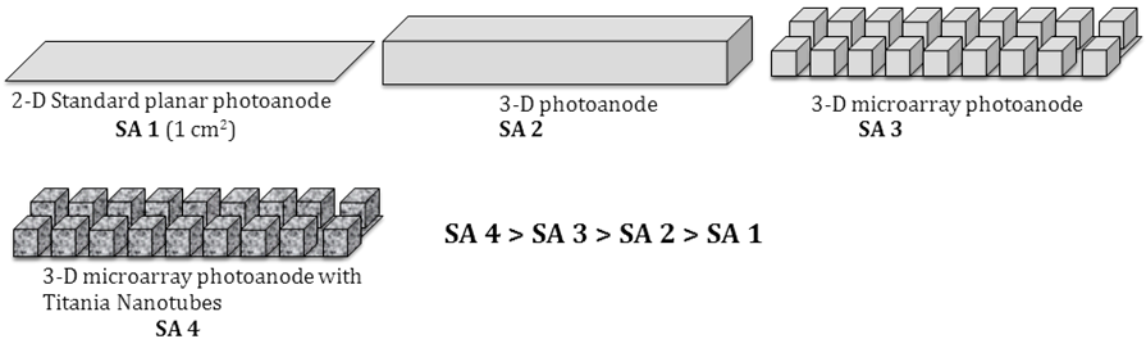

Figure 3.3. Illustration of the increase from 1 cm sq. surface area using microarray of 3-D structures.

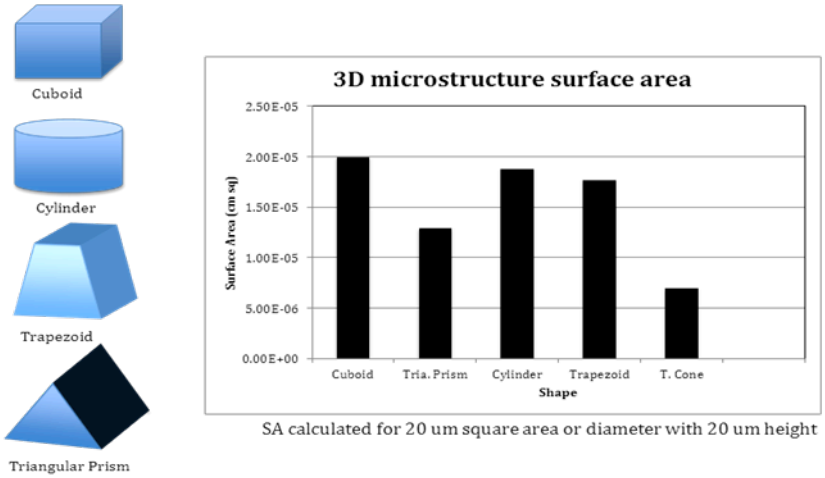

Figure 3.4. An example of shape and surface area given set dimensions for each. The cuboid gives the most followed by the cylinder then the trapezoid.

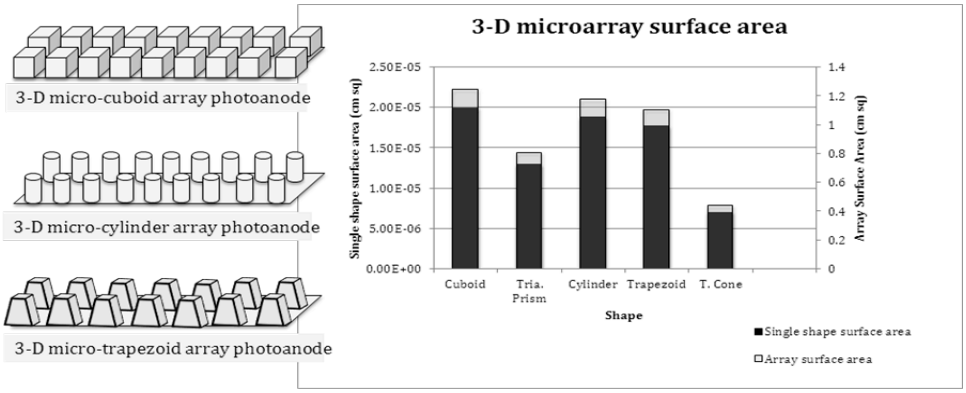

Figure 3.5. Example of surface area of a 3-D microarray photoanode.

into two main areas: surface and bulk micromachining. Surface micromachining begins at the surface of the substrate and follows a bottom-up approach in the fabrication of micro-components. In contrast, bulk micromachining starts from the surface and proceeds into the

surface of the substrate following a top-down fabrication approach. Photolithography is applied in both of these areas, and uses light and a metal-coated glass stencil to selectively pattern photosensitive polymers (photoresists) that are coated onto the surface of a substrate. The resist can either be a temporary chemical resistive layer for bulk micromachining via substrate etching or can be a final permanent component of the microdevice. Photoresists such as polymethyl methacrylate (PMMA) and SU-8 are used extensively in MEMSs and HARMSTs as permananent high-surface area microsystem components. Other less conventional polymers such as polydimethlysiloxane (PDMS) are increasingly becoming more utilized for microfluidic devices and flexible film applications.

3.2.1 Photolithography

Figure 3.6 is a cross-sectional illustration of the fabrication process. Silicon dioxide wafers (p-type, <100>) were spin-coated with SPR 220 7.0 positive photoresist (Rohm and Haas) using a light-duty photoresist spinner. The wafers were baked on a hotplate, then UV exposed in mask contact mode using an optical photomask. The photomask was patterned with 1 cm x 1 cm areas of arrays of circles and squares of varying dimensions ranging from 5 to 20 μm. The exposed wafers were then post-exposed baked and developed in MF-319 Developer (Shipley) to produce the resist patterns.

3.2.2 Etching: Surface and Bulk

Before bulk etching of the silicon can occur, selective surface etching of the exposed silicon dioxide surface areas was performed. First, a resist hard-bake step was done to render the resist harder to remove during the surface etching process. The silicon dioxide windows were etched using a 10:1 H_2O:HF buffered oxide etchant (BOE) or reactive ion etching (RIE in the case for silicon nitride films).

For 3-D surface-texturing, the trapezoidal profile shape is preferred because (1) the inclination of the sidewalls provide for nearly conformal-like coating of subsequent thin-film coatings, and (2) the trapezoidal shape is attainable via anisotropic wet etching of <100> silicon.

Wet bulk etching of silicon can result in two types of profiles, isotropic and anisotropic depending on the crystal lattice orientation of the exposed surface. Figure 3.7 illustrates the two profile types. Three crystalline planes (<100>, <111>, <110>) are considered when etching. Wet etching of the <100> plane using a heated potassium hydroxide (KOH) bath results in the preferred trapezoidal profile shape of the bulk silicon. As shown in Figure 3.7, a 54.7° angle of sidewall inclination from the silicon surface is attained. All planes are etched, however the etching rates for the different planes are different. In a heated KOH bath, the etching rate for the <100> plane is faster than that of the <111>, or <110> planes.

The etching solution was 30% KOH in de-ionized water at 65°C. The etching time depended on the pattern dimensions and ranged from 5 min to 30 min. After etching, the samples were rinsed in an ultrasonic bath of warm de-ionized water.

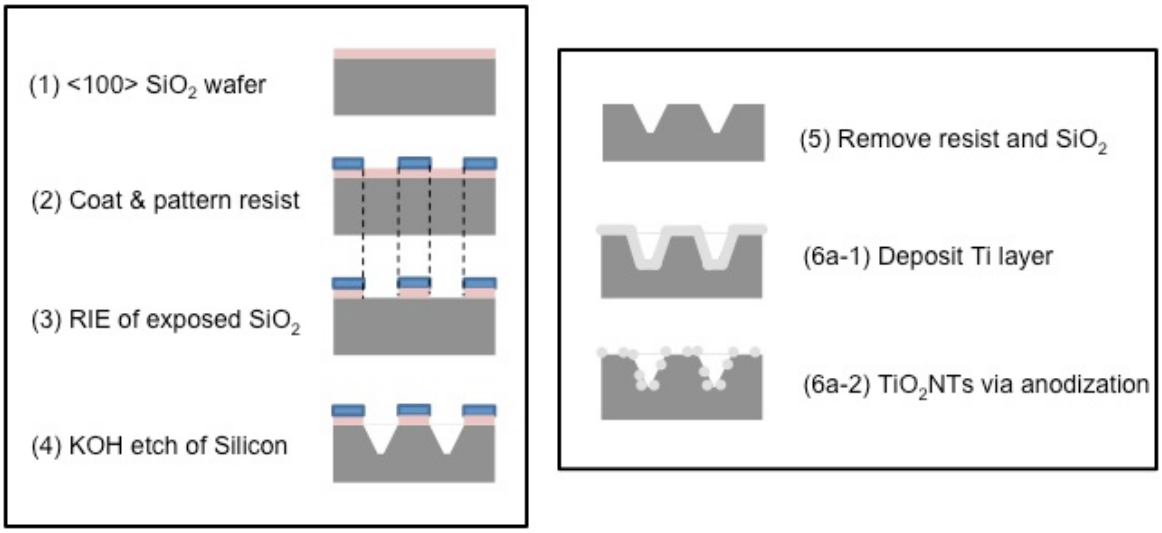

Figure 3.6. Schematic illustration of the 3-D hierarchical micro-nanostructure fabrication process on silicon.

3.3 Results and Discussion

Scanning electron microscopy (SEM) was used to observe the 3-D etched silicon microstructures. Figure 3.8 is an example of some of the etched samples. Figure 3.9 is an image of the type of microwell array used for further investigation. The microwells are 10 μm^2 x 15 µm deep with a pitch of approximately 2 µm.

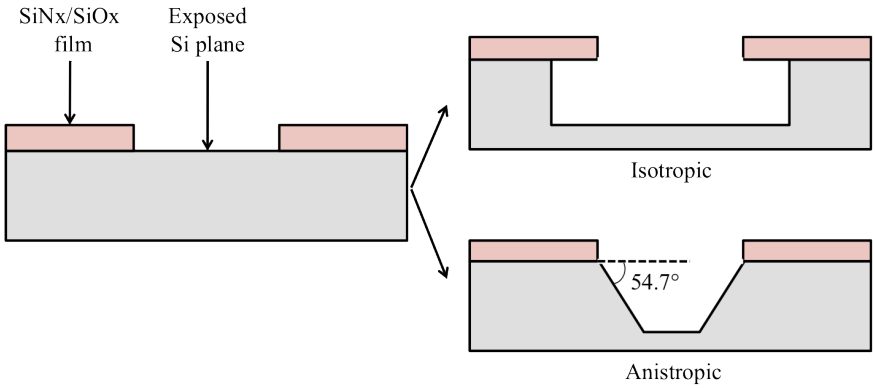

Figure 3.7. Illustration of isotropic and anisotropic wet etching profiles of silicon.

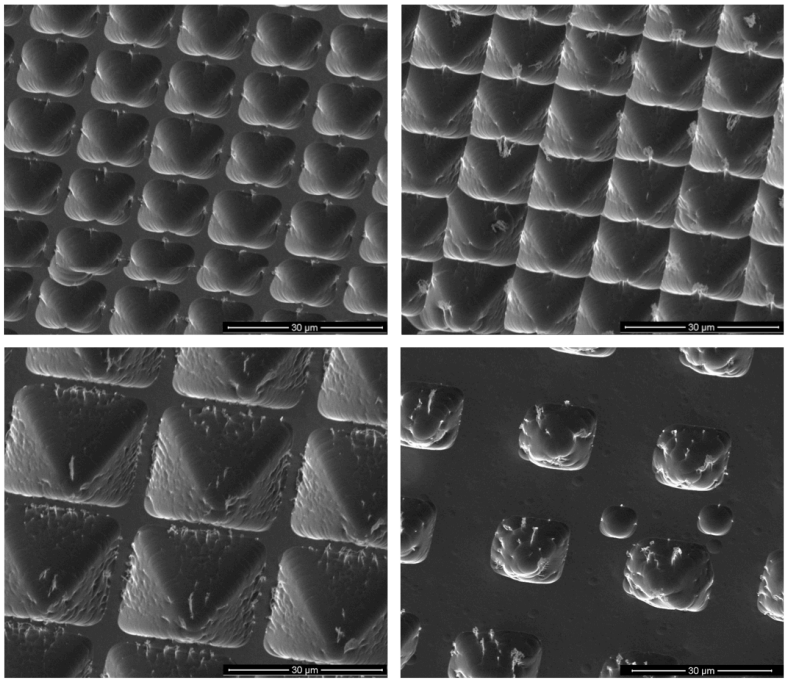

Figure 3.8. SEM images of Si-etched microwells of varying dimensions.

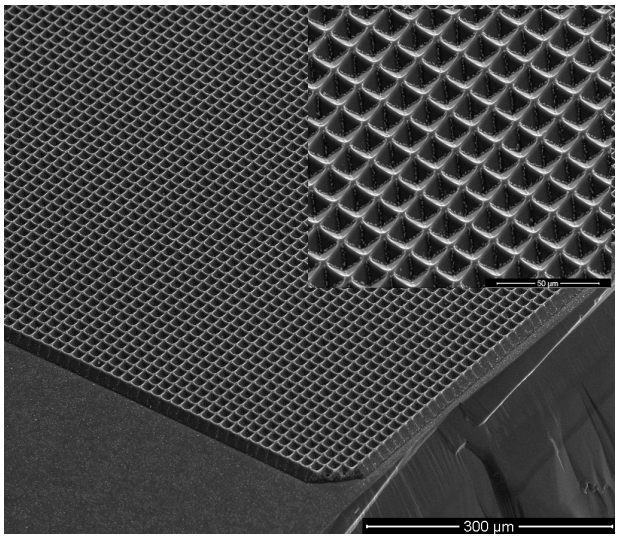

Figure 3.9. SEM images of micro-wells etched in silicon. Scale bar of the insert is 50 µm.

3.4 Summary

The 3-D shapes naturally have more surface area than their 2-D counterparts. Designing the 3-D photoanode using photolithography has limitations but has its advantages. The limitations are based on that the final 3-D structure arises from a 2-D pattern. There are techniques, which may provide more elaborate and intricate 3-D shapes. The advantages of using photolithography are the myriad of 2-D pattern variations possible limited only by your imagination and instrumentation. The 3-D shapes may be made of various materials including photosensitive polymers, electroplated metals, silicon-etched molds, metal and polymer composites, rigid and flexible polymers, etc. However, consideration of the subsequent processes for metal thin film formation of a photoanode must be given. Of the basic shapes selected, the trapezoid provided a surface for conformal-like coating of Ti thin-film via DC magnetron sputtering. The trapezoid is also ideal in that it (and its multi-sided variations) is a shape obtained from KOH anisotropic etching any 2-D pattern on <100> oriented silicon. Here, the smallest lateral area feature was 10 μm^2 with pitch variation between array elements ranging from no pitch to 10 µm. The depth reached at most was 15 µm. These shapes are similar to the

inverted pyramidal surface-texturing technique utilized in the high-efficiency Si-based PERL solar cells [2].

3.5 References

[1] Shipley Microposit S1800 Series Data Sheet. Available at http://nanofab.ece.cmu.edu/resources/. Accessed on 1/16/14.

[2] M. Green, Silicon Solar Cells: Advanced Principles and Practice. Centre for Photovoltaic Devices and Systems, Univ. of New South Wales, Sydney, 1995.

CHAPTER 4. FORMATION OF TITANIA NANOTUBE FILM

4.1 Introduction

Figure 4.1 is an illustration of a titania nanotube with a moderate height dimension of 500 nm, 150 nm outer diameter and a 100 nm inner diameter. The surface area of the cuboid, cylinder, and trapezoidal microarray more than doubles when these predefined nanotubes are grown on them. It is also of interest to note that given the moderate dimensions of the 3-D microstructural array allows area for more than 1 billion nanotubes. Figure 4.1 also explores the possibility of forming 1000 nm (1 μm) tall nanotubes on a more condensed array arrangement resulting in a 7X gain in surface area. In this arrangement, there is no gap between the elements in the trapezoidal array and a minimum gap (5 μm) between the elements of the rectangular cuboid and cylindrical arrays.

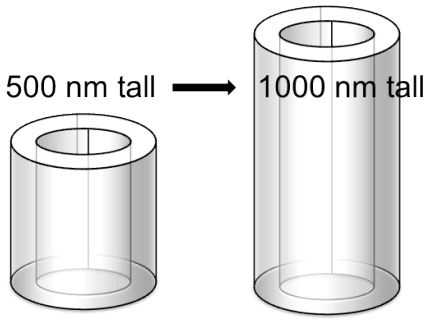

PA TYPE	*SA (cm^2)	*SA (cm^2) Condensed + TiNT height	**SA (cm^2) Condensed HARMS + TiNT height
R. Cube array	4.56E+01	2.25E+02	3.21E+02
Cylinder array	4.51E+01	2.17E+02	2.89E+02
Trap. Pyra array	4.34E+01	2.04E+02	3.09E+02
STD CELL	2.28E+01	4.5E+01	4.5E+01
	~2X SA	~5X SA	~7X SA

*within a 1 cm sq lateral area, aspect ratio of 1.
**within a 1 cm sq lateral area, aspect ratio of 1.6

Figure 4.1. Illustration and examples of the increased surface area and approximate number of nanotubes that will fit on a 3-D microarray photoanode.

4.2 Experiment

4.2.1 Preliminary Study on Ti Foil and Wire Formats

To verify literature [1-3] and testing setup for the formation of TiO_2 nanotubes, a preliminary study of the anodization of commercially available Ti foil and wire was performed.

Sheets of Ti foil (99.96%) with a thickness of 25 μm were cut into 1 cm^2 samples. The wire used was 0.5 mm in diameter and 1 cm in length. An electrolyte solution was prepared using a mixture of 200 mL of ethylene glycol (EG, $C_2H_6O_2$), 0.685 g of sodium fluoride (NH_4F) and 4.4 mL of de-ionized water. This solution was allowed to mix for 20 min. before use. Anodization was performed using a two-electrode electrochemical system with a platinum (Pt) disc as the cathode and the Ti foil/wire as the anode. The anodizing parameters were set at 60 V at constant current under room temperature. Different anodizing times were performed to see the evolution of TiO_2 nanotube formation. It was observed that the color of the foil surface changed during the formation of the nanotubes beginning with blue then gradually changing to yellow, red, and bright green.

Scanning electron microscopic (SEM) images of the nanotube formation are shown in Figure 4.2. In only five minutes, 30 μm tall, vertically oriented TiO_2 nanotubes were formed. The final film thickness was 5 μm more than originally due to the oxide thickness formed. The film also was visibly transparent. From a cross-sectional analysis of the anodized film, the tubular structure can be seen. In the right of Figure 4.2 is an illustration of the nano-tubular cross-section. Confirmation of the formation of nanotubes around the cylindrical-shaped Ti wire is shown in Figure 4.3. This preliminary study thus verifies that formation of high-surface area TiO_2 nanotubes via the in-house experimental setup and as described under literary reported conditions is feasible on flat as well as on cylindrical surfaces. It is now of interest to form such TiO_2 nanotubes within a thin Ti film on 3-D microstructures.

4.2.2 Titanium Thin-Film Deposition by Sputtering

In order to obtain TiO_2 nanotubes on 3-D silicon microstructures, it is key that a deposition method is chosen that will (1) provide good interfacial adhesion, and (2) result in a

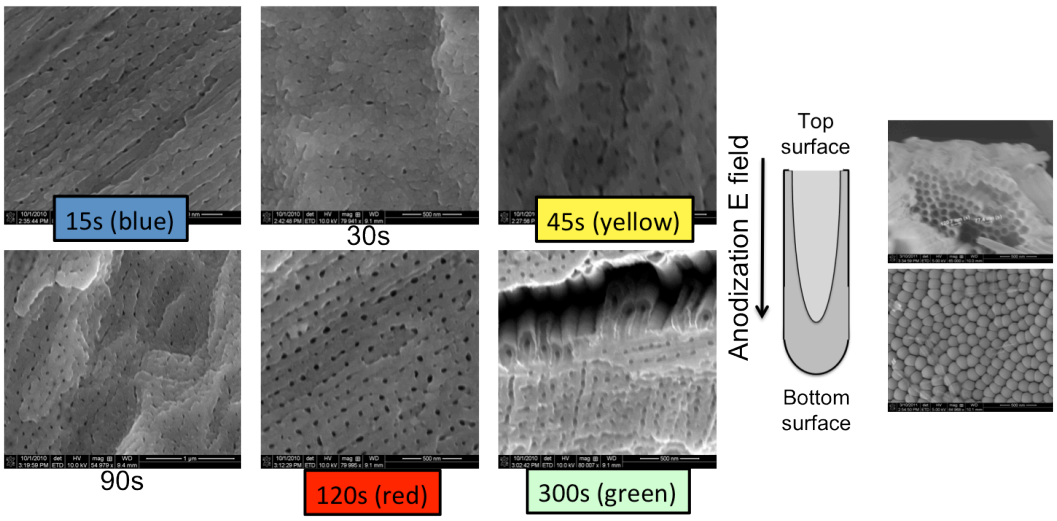

Figure 4.2. SEM surface analysis of the formation of TiO_2 nanotubes at different times. An illustration of the tubular cross-section and top and bottom is also shown.

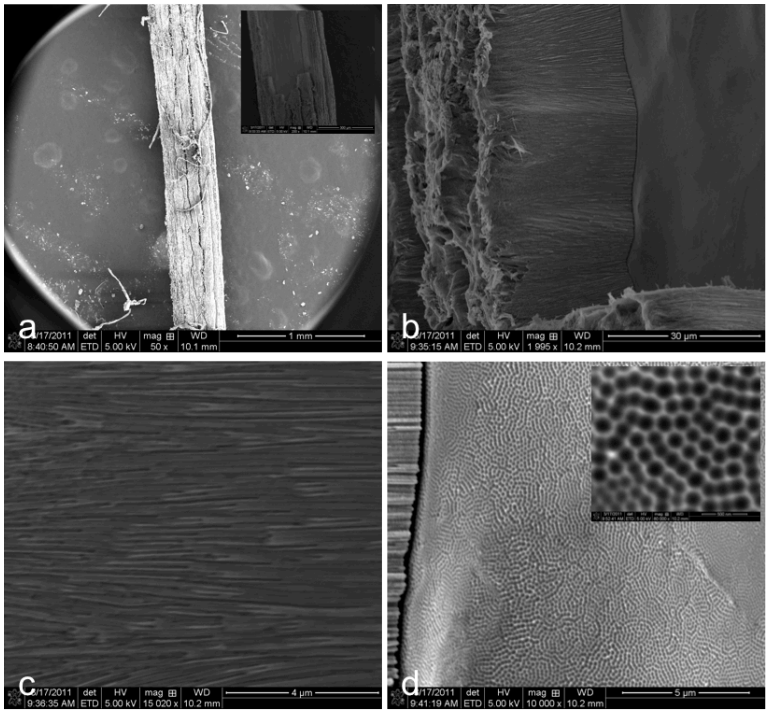

Figure 4.3. SEM surface analysis of the formation of TiO_2 nanotubes on a Ti wire showing a) the anodized wired with an in-set showing a cracked area, b) an enlarged view of the cracked area, c)side view of nanotubes, and d) top of cracked surface showing a continued anodized surface.

conformal-like coating on the 3-D non-planar surface. Several thin-film deposition techniques are available [4]. Electro-less deposition methods are useful for uniformly coating non-conductive non-planar and planar surfaces. There is a limitation on the types of metal ionic

baths that are available for electroless plating. Currently, titanium is not a metal capable of electroless deposition. Vacuum coating methods such as sputtering is useful when the target substrate is conductive. It is possible to sputter insulative materials but poisoning and charge build-up on the surface can occur. Furthermore, sputtering uses accelerated charged ions of the chosen material to bombard the target substrate. This bombardment implants the sputtered material into the target substrate physically deforming the target material. Another vacuum coating technique is evaporation. Under vacuum, the deposition material is heated in a crucible sitting below the target substrate until the vapor pressure becomes substantial causing the atoms of the heated material to evaporate. The atoms evaporate upwards into the vacuum chamber where they are deposited onto the target's surface. This method does not require a conductive target. As with the other techniques, adhesion of primary materials may be assisted by other materials. Evaporation however allows flexibility of substrate mounting and also gives the opportunity to produce conformal-like coatings.

Initially, the evaporation technique was utilized since it is ideal for future studies on the development of 3-D photoanodes on non-conductive thin-film polymer formats such as SU-8, PMMA, and polyimide. However, due to equipment failure, the sputtering technique was used as an alternative. Appendix B details the methods and findings using e-beam evaporation on silicon and polymer.

Prior to thin-film deposition, a second BOE/RIE step was performed to remove the excess silicon dioxide/nitride. Then the substrate was cleaned by rinsing with acetone, followed by IPA, and de-ionized water then dried with nitrogen and dehydrated in a convection oven at 100 °C for 2 hours. The substrates were then diced into ~1.2 cm^2 silicon chips. The 3-D microstructured arrays were conformally-like deposited with titanium via DC magnetron

sputtering (Oxford). The varied sputtering parameters were DC power of 120 W, 160 W, and 180 W all under a working pressure of 1 mtorr, with Argon as the carrier gas at a flow rate of 20 – 30 sccm. Typically, deposition via sputtering results in amorphous titanium, and subsequently amorphous titania due to the formation of the native oxide once removed from the chamber.

4.2.3 Anodization of Titanium Thin-Film

Titanium (Ti) is a transitional metal of the periodic table. 22 electrons surround each atom with two valence electrons in the fourth outer-most energy level. These valence electrons are readily available for bonding to other metals, which is why Ti is classified as a transitional metal. Ti has a hexagonal close packed (hcp) crystal lattice structure with a lattice constant of 2.95 Å. It readily and naturally oxidizes when exposed to air forming a 1–2 nm thick titanium dioxide (TiO_2) passivation layer. This oxidized film is an n-type semiconductor. Among many ways to oxidize Ti, anodization via an electrolytic solution is a relatively easy and controlled way to form TiO_2. Using a setup as illustrated and pictured in Figure 4.4, this method has also been found to form high-surface area TiO_2 nanotubes oriented perpendicular to the surface of titanium [5-7]. This formation of TiO_2 nanotubes occurs through a process known as pitting corrosion, an oxidation-reduction (redox) process [8].

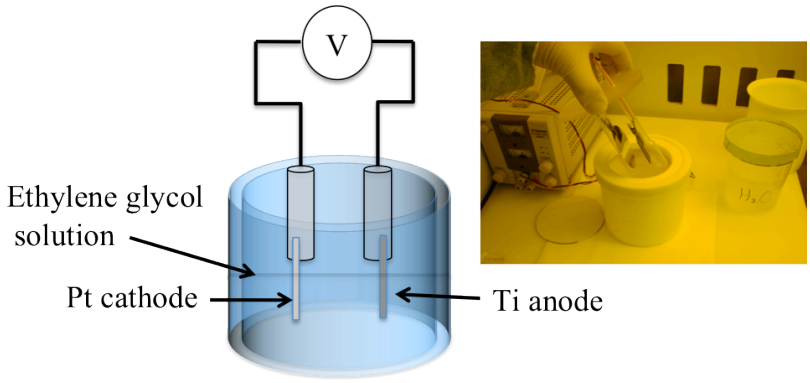

Figure 4.4. An illustration and actual setup for electrochemical anodization of Ti.

Anodization is an electrochemical method that forms an oxide layer on a substrate [5-10]. In anodizing titanium, a visual color change is apparent with the color dependent on the thickness of the oxide layer. This color is also indicative of a structural change of the surface of the metal. Grimes et al. [11] discovered that under a potential with acidic or organic electrolytes, the structural change observed for titanium revealed structures on the nanoscale.

4.3 Results and Discussion

4.3.1 Titanium Thin-Film Adhesion

The films deposited under the various DC power sputtered conditions all passed the tape adhesion test [12], thereby exhibiting sufficient film-to-substrate adhesion. Adhesion of thin-film titanium deposited by e-beam evaporation typically requires an adhesive layer such as chromium and/or gold to aid in the adhesion of the titanium to silicon (see Appendix B). Although such films may also be utilized as electron transfer mediums, the titanium films deposited via sputtering did not require them.

The root mean square (RMS) value of the average profile roughness of the 160 W sputtered sample was 1.349 nm. This deposition resulted in a smoother surface profile than the 120 W and the 200 W deposited films with RMS average roughness values of 2.259 nm and 2.604 nm respectively. Figure 4.5 is SEM images of the 120 W, 160 W, and 200 W surfaces. In comparison, the commercially available titanium foil has an RMS value of 27.89. The roughness of the foil is larger most likely do to large cracks present in the foil. In comparison, the sputtered film surface roughness is more uniform than the foil. In Figure 4.6, SEM images of both of these surfaces are shown for comparison.

As observed from the SEM images in Figure 4.7, sharp etched edges are rounded and smoothened out after the titanium deposition. This is ideal since stress at sharp edges results in

cracks within the nanotube film. To clearly see the Ti film deposition on the 3-D surface, SEM images were taken of the array viewed from the top (Figure 4.8a), then tilted at a 52° angle (Figure 4.8b), and magnified to a cross-section of the wells (Figure 4.8c and Figure 4.8d).

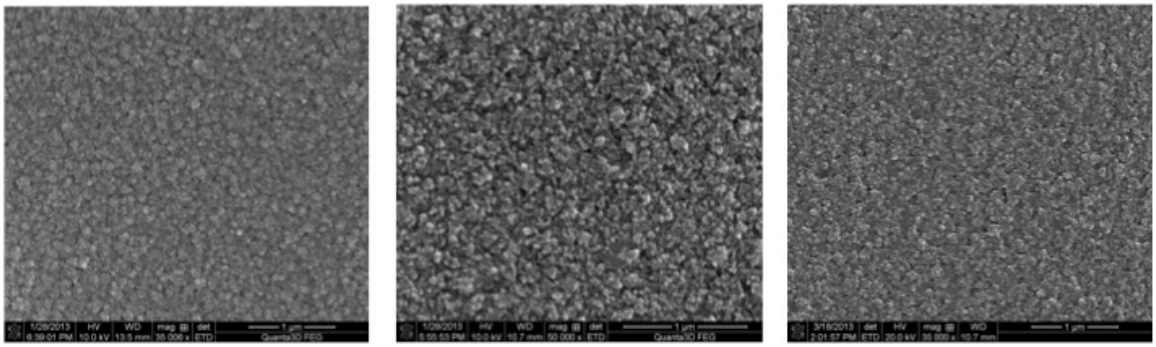

a) b) c)

Figure 4.5. SEM imaged of as-sputtered Ti films at a) 120, b) 160, and c) 200 W.

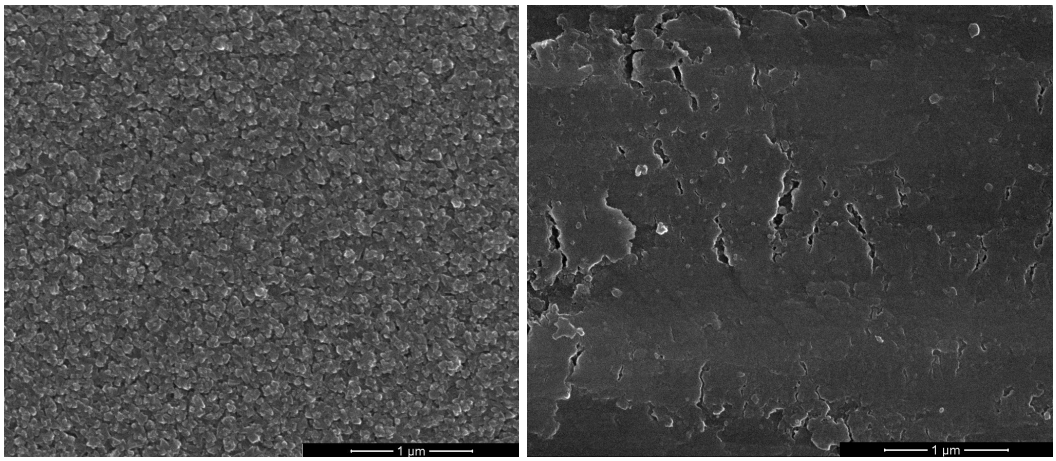

(a) (b)

Figure 4.6. SEM image of as-deposited sputtered titanium thin-film at DC power of (a) 160 W, vs (b) as-purchased Ti foil [13].

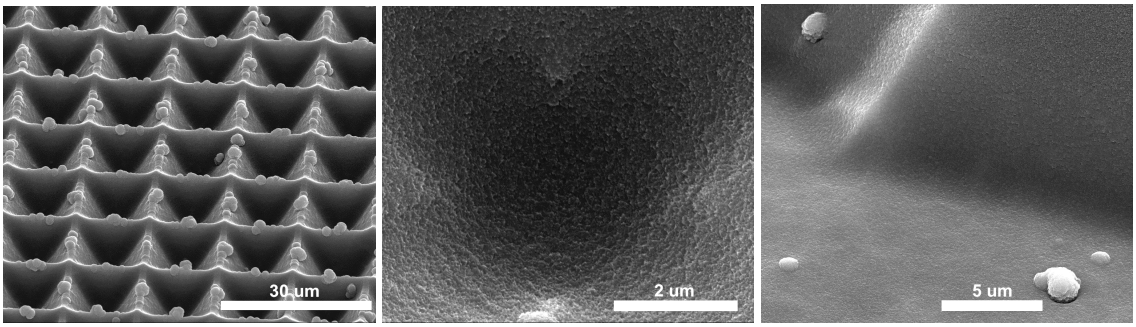

Figure 4.7. SEM images showing the titanium deposition over the microarray of silicon wells [13].

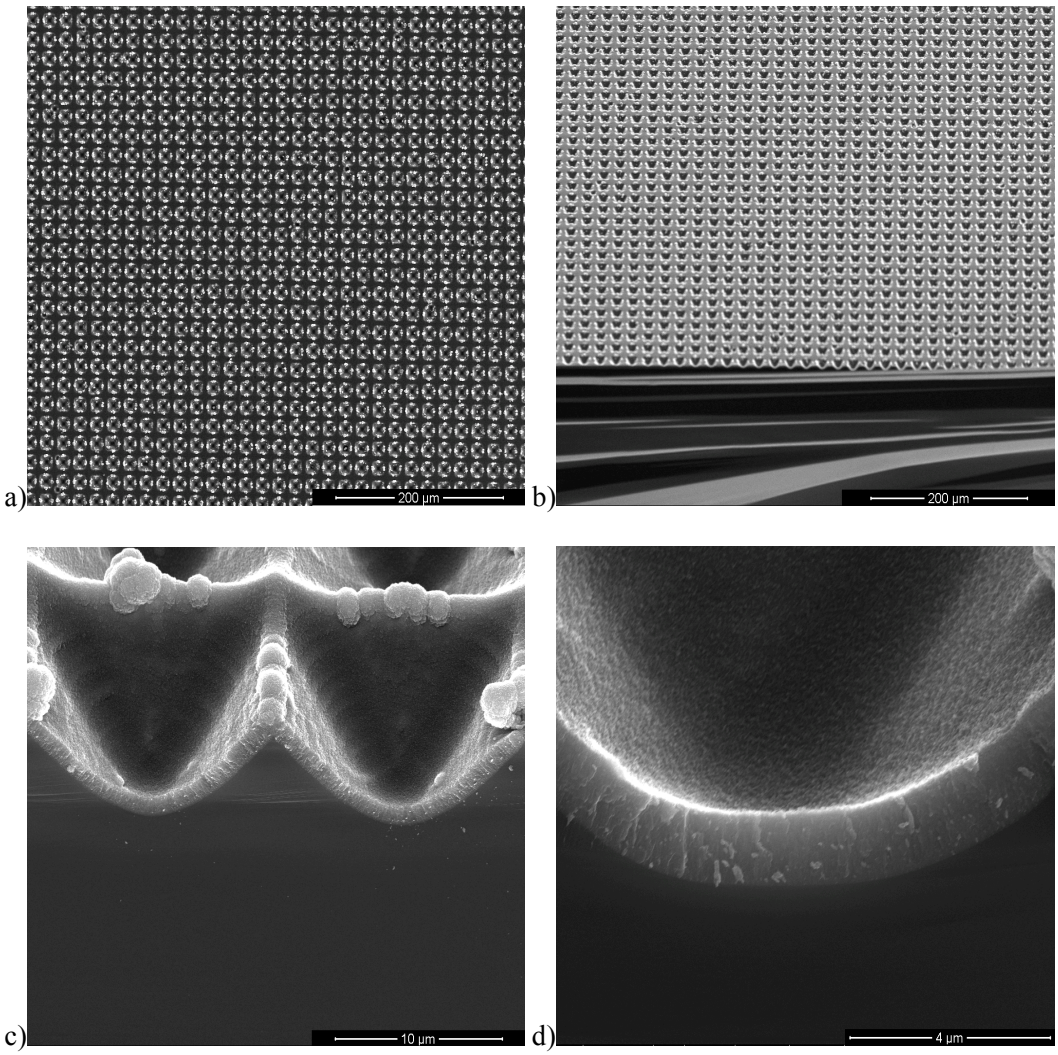

Figure 4.8. SEM images post-anodization showing a) the micro-array of wells from the top, b) viewed from a 52° angle, c) profile of the wells, and d) magnified view of the profile showing a conformal-like titanium coating of the 3-D microwell [13].

These figures are evidence of the conformal-like deposition of titanium thin-film on the 3-D microstructure. The microstructures shown are an array of 15 μm^2 x 15 µm-deep wells with a 2 µm pitch. The 1 cm^2 cell area has 443,556 (array of 666 X 666) wells.

4.3.2 Surface Area Enhancement

Figure 4.9 shows the deposited titanium film post-anodization. The cross-section shown above is along the edge of the well. Nanotubes by anodization form perpendicular to the surface and are not visible along this cut edge. Imaging from the top surface to the bottom of the micro-

well as shown in Figure 4.9, TiO_2 nanopores are observed around the inner surface of the entire micro-well wall.

Figure 4.10 shows the cross-sectional view taken at the center of the well. TiO_2 nanotubes, approximately 340 nm in height with outer and inner diameters of 180 nm and 75 nm respectively, are clearly observed. Given these nanotube dimensions, there are approximately 3,300 nanotubes within one micro-well.

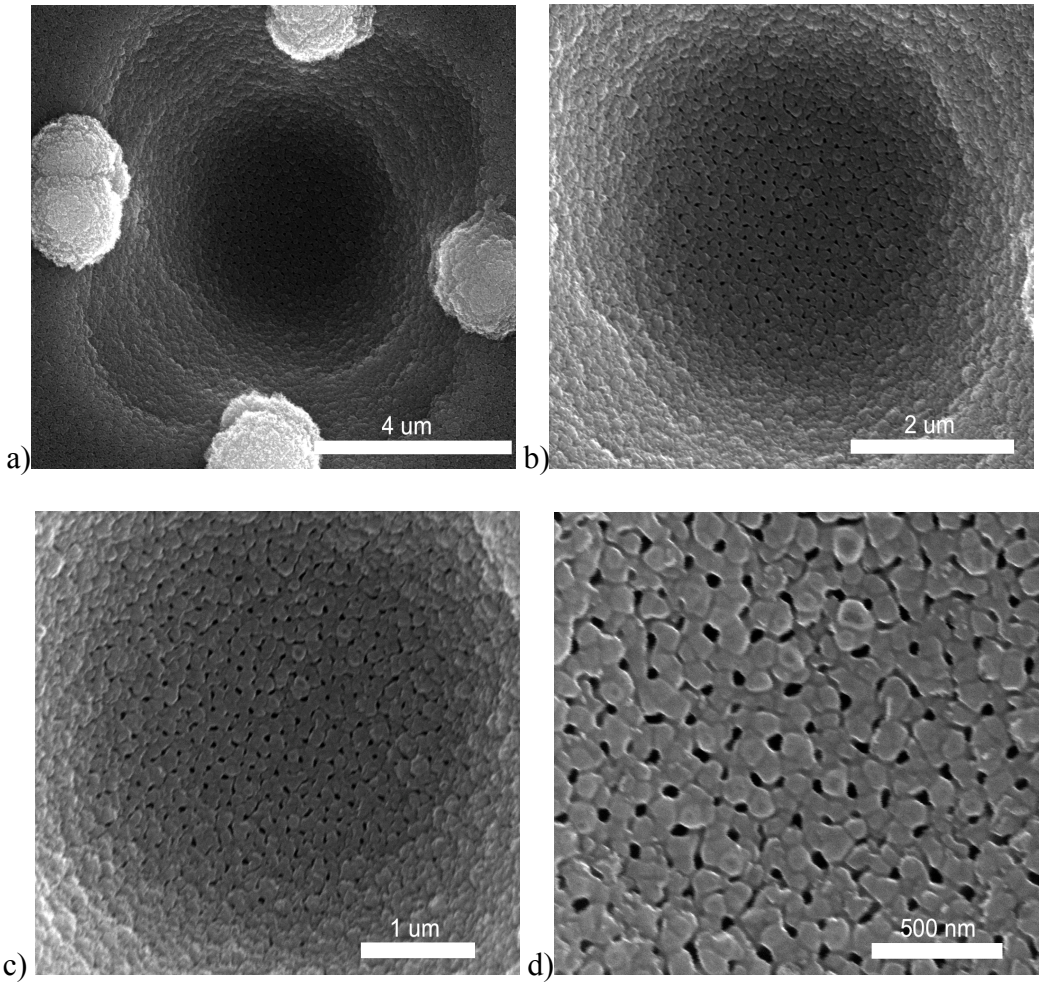

Figure 4.9. SEM images showing the formation of TiO_2 nanotubes alongside the inner surface of the micro-well at (a) 4 μm, (b) 2 μm, (c) 1 μm, and (d) 500 nm scale bars [13].

Therefore, including the surface between each well, each 1 cm^2 cell has about 2.4 billion nanotubes. The approximate total surface area of the nanotube layered 3-D microstructured

photoanode then is 7.85 cm^2. This is more than 7 times the surface area of a planar photoanode and more than 5 times the surface area of a nanotube film enhanced flat photoanode. Also shown in Figure 4.10 is an illustration of the cross-sectional view of a single nanotube. Given the directional electric potential field (E)-assisted anodization of the titanium thin-film, the nanotubes are formed via an electrochemical reduction-oxidation (redox) process resulting in an open top and capped bottom.

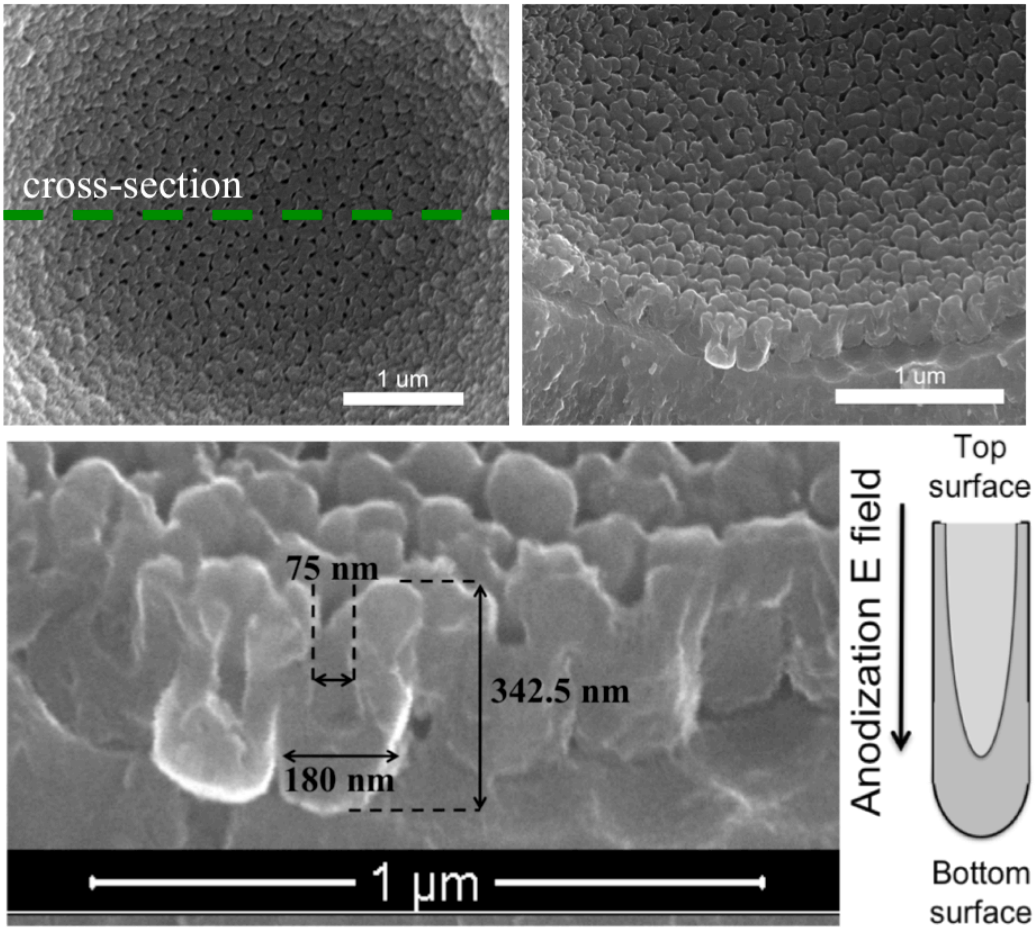

Figure 4.10. SEM images taken of the cross-sectional view through the center of a micro-well showing the nanotubes [13].

4.4 Summary

Surface area of the 3-D silicon etched microwells was increased by the formation of TiO_2 nanotubes within a sputtered Ti thin-film using anodization. Film deposition by magnetron

sputtering resulted in films with a conformal-like coating on the textured surface. Unlike depositions initially sought out via e-beam evaporation, obtaining the conformal coating of the films did not require a tilt-and-rotate mechanism. Adhesion of the film was also improved and did not require the aid of an adhesive layer. The roughness of the deposited films appeared to play a role in the formation of nanotubes. Under the constant conditions of the electrochemical setup, nanotube formation was only observed in films with an approximate RMS value of 1.35 nm deposited under a power of 160W. The nanotubes were formed within 5 minutes of anodization and resulted in dimensions of approximately 340 nm in height with outer and inner diameters of 180 nm and 75 nm respectively. Along the microwell walls, the nanotubes are formed perpendicular to the surface.

4.5 References

[1] D-J. Yang, H-G. Kim, S-J. Cho, and W-Y. Choi, Vertically Oriented Titania Nanotubes Prepared by Anodic Oxidation on Si Substrates, IEEE Transactions on Nanotechnology, 2008, Vol. 7, No. 2, 131.

[2] G. K. Mor, O. K. Varghese, M. Paulose, K. Shankar, C. A. Grimes, A review on highly ordered, vertically oriented TiO_2 nanotube arrays: Fabrication, material properties, and solar energy applications, Solar Energy Materials & Solar Cells, 2006, 90, 2011–2075.

[3] B. Chen, Lu, K, Influence of Patterned Concave Depth and Surface Curvature on Anodization of Titania Nanotubes and Alumina Nanopores, Langmuir, 2011, 27, 12179-12185.

[4] D. M. Mattox, The Foundations of Vacuum Coating Technology, Elsevier, 2003.

[5] K.S. Raja, M. Misra, K.Paramguru, Formation of Self-Ordered Nano-Tubular Structure of Anodic Oxide Layer on Titanium, Electrochimica Acta, 2005, 51, 154-165.

[6] H. E. Prakasam, K. Shankar, C. A. Grimes, A New Benchmark for TiO_2 Nanotube array Growth by Anodization, Journal of Physical Chemistry C, 2007, 111, 7235-7241.

[7] C. W. Lai, S. Sreekantan, Effect of Applied Potential on the Formation of Self-Organized Nanotube Arrays and Its Photoelectrochemical Response, Journal of Nanomaterials, 2011, doi:10.1155/2011/142463.

[8] G. K. Mor, O. K. Varghese, M. Paulose, C. A. Grimes, Transparent Highly Ordered TiO_2 Nanotube Arrays via Anodization of Titanium Thin Films, Advanced Functional Materials, 2005, 15, 1291–1296.

[9] M. Remškar, Inorganic Nanotubes, 2004, Advanced Materials, 16, 1497–1504.

[10] Http://en.wikipedia.org/wiki/Anodizing. Accessed on 9/15/12.

[11] C. Grimes, Synthesis and Application of Highly Ordered Arrays of TiO_2 Nanotubes, J. Mater. Chem., 2007, 17, 1451–1457.

[12] ASTM D3359-02, Standard Test Methods for Measuring Adhesion by Tape Test, 2002

[13] F. Dawan, N. Morampudi, Y. Jin, E. Woldesenbet, Hierarchical Fabrication of TiO_2 Nanotubes on 3-D Microstructures for Enhanced Dye-Sensitized Solar Cell Photoanode for Seamless Microsystems Integration, Journal of Microelectronic Engineering, doi: http://dx.doi.org/10.1016/j.mee.2013.10.007S.

CHAPTER 5. CHARACTERIZATION OF NANOTUBE FILM-ENHANCED (NFE) PHOTOANODE

5.1 Introduction

As mentioned in Section 2.1, the photoanode is one of the major components of a solar cell. It is the central hub for light absorption and photon-electron conversion. Therefore, understanding the material composition, and the fundamental optical and electrical properties of the photoanodes is important in photovoltaic applications.

Here in this chapter, a discussion and method of altering the photocatalytic polymorphs for TiO_2 is given. To increase the light absorption sensitivity of the photoanode, coating of the photoanode with a dye-sensitizer is also performed. Grazing incidence angle x-ray diffraction, spectrum reflectance, dye-loading capacity, and current density measurements including degradation of the NFE 3-D photoanode were performed and compared to its flat counterpart.

5.2 Experiment

5.2.1 Annealing of TiO_2 Thin-Film

TiO_2 exists in an amorphous state and crystalline state. The crystalline state is present in mainly three phases: brookite, anatase, and rutile. The brookite phase is an unstable phase and is rarely present, whereas the metastable (unstable and transient energy state) anatase and stable rutile phases are more common. These two phases are applicable to photovoltaics as they both have photocatalytic properties. As with photovoltaic material, photocatalytic material produces e-h pairs under illumination. It has been reported that the anatase phase of TiO_2 has improved photocatalytic performance due to its higher surface area and smaller microstructure grain size compared to the rutile phase [1]. This higher surface area provides more sites for the generation of e-h pairs. The smaller grain size increases the probability of electron and hole trapping which reduces e-h pair recombination [1]. The band gap energy required to generate an e-h pair in

anatase TiO_2 is 3.2 eV (about 380 nm), and is 3.02 eV (300 nm) for rutile [1]. When using DC magnetron sputtering, as-deposited titanium is in the amorphous form, which has no photocatalytic properties. Altering the phase of TiO_2 can be achieved chemically or thermally through an annealing process.

Annealing is a type of heat treatment that can alter the phase and/or microstructure of a metal. Amorphous TiO_2 transforms into anatase TiO_2 between temperatures of 200 and 500 °C at atmospheric pressure (1 atm). Rutile TiO_2 is achieved at temperatures greater than 500 °C. Typically, a pure phase of TiO_2 is not present and instead the material consists of a mixture (anatase and rutile) of phases.

The as-deposited anodized films were annealed to transform the amorphous nanotube film into a highly crystalline anatase and rutile phase nanotube film. Annealing was performed in ambient (1 atm) conditions at 450 °C using a high-temperature oven (Thermolyne).

5.2.2 Grazing Angle X-Ray Diffraction

Grazing incidence angle x-ray diffraction (GID) was performed to analyze the presence of phases. This characterization technique is well suited for phase analysis of thin-films over the conventional method. Figure 5.1 is an illustration showing the difference between GID and conventional x-ray diffraction (XRD). The x-ray angle of incidence in conventional XRD systems is usually high with respect to the sample's surface resulting in deeper penetration of the x-rays into the material. Therefore phase analysis information of the surface is not clearly distinguished from the bulk or other possible layers. In GID, the angle of incidence is much lower with respect to the sample's surface, which increases the x-ray path length within the thin-film resulting in distinct thin-film phase information [2-3].

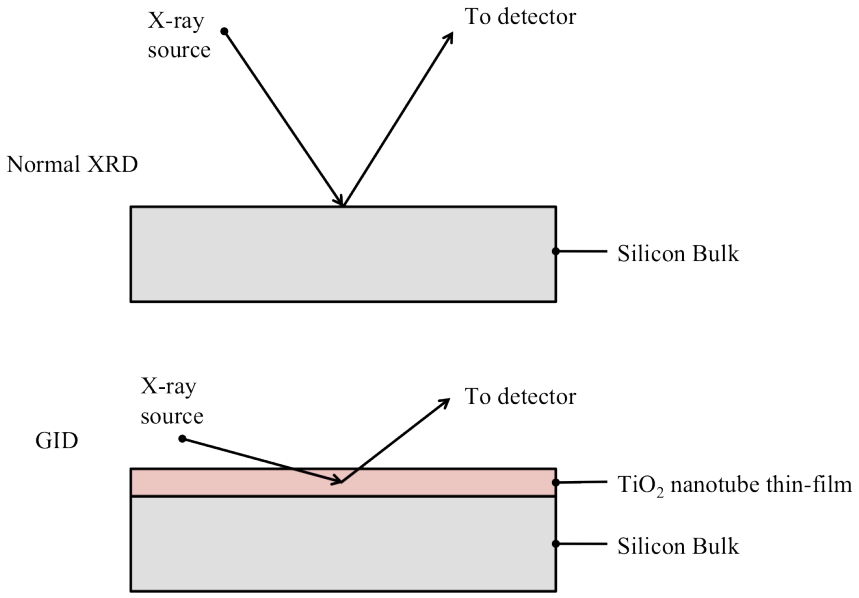

Figure 5.1. Illustration of normal XRD versus GID [2-3].

Grazing incidence diffraction measurements were conducted at the Bruker facility using the D8 Discover with DAVINCI design. The sample was probed with a submicron spot source at a 5^{o} incident angle where y = 0^{o} and 90^{o} respectively and data acquisition was collected using two methods: (1) the 1D Lynseye and (2) the 2D VANTEC-500 area detector at a 0.04^{o} step size.

5.2.3 Dye-sensitization of the NFE Photoanode

0.3 mMol of N719 dye was dissolved in ethanol and thoroughly mixed. The samples were soaked overnight in this solution and allowed to dry. To get an image of the dye-film, scanning electron microscopy (SEM) was performed of the dry dye film on a flat sample. The dye-sensitized NFE flat and 3-D surface-textured samples were then characterized for their optical and electrical properties.

5.2.4 Fiber Optic Spectrophotometry

The dye-loading capacity and light absorption properties were measured using an optical fiber spectrometer (HR2000+, Ocean Optics). The dye absorption spectrum is shown in Figure 5.2. N719 is a commercially available ruthenium-complex-based dye that peaks at a wavelength

of about 535 nm. 0.3 mMol of N719 dye was dissolved in ethanol and thoroughly mixed. The samples were soaked overnight in this solution and allowed to dry. To get an image of the dye-film, scanning electron microscopy (SEM) was performed of the dry dye film on a flat sample. To evaluate dye-loading capacity, fingerprint absorption spectra for 0.3 mMol and subsequent dilutions were taken. NFE flat and 3-D surface-textured dye-sensitized samples were then soaked in ethanol solutions under sonication to remove the adsorbed dye after which an absorption spectrum of each solution was taken. This spectrum was then compared to the fingerprint spectra to determine the adsorbed dye molar concentration per sample area. The Variable-Angle Reflection Sampling system (VARS, Ocean Optics) was used to determine the reflectance of bare silicon, 3-D surface textured silicon, NFE flat, NFE 3-D, and dye-sensitized NFE flat and 3-D samples. Surface texturing can increase the optical path length of an incident beam. Figure 5.3 is an illustration of this property. The NFE 3-D surface further increases the optical path length of an incident beam due to the multiple nanotubular surfaces in addition to the surface texturing the beam encounters. Annealing of the nanotube film increases the degree of crystallinity of the nanotubes. Furthermore, titania has high index-of-refraction properties of up to 4.372 for wavelengths at 300nm [4]. Figure 5.4 is a wavelength dependent graph of the index of refraction for anatase-titania. Titanium is shown as a reference. Anatase titania has a very high index of refraction which is ideal in trapping light from a low-index of refraction medium such as air which has an index of refraction value of 1. Figure 5.5 illustrates the possible refractive paths a beam incident on a high-refractive-index nanotubular wall may take. Here, consideration is only given to light interaction with titania nanotubes. Layers prior to this are not relevant to the photo properties of the photoanode and only serve as a fabrication platform. However, reflectance of light from the platform will be factored into the performance. The

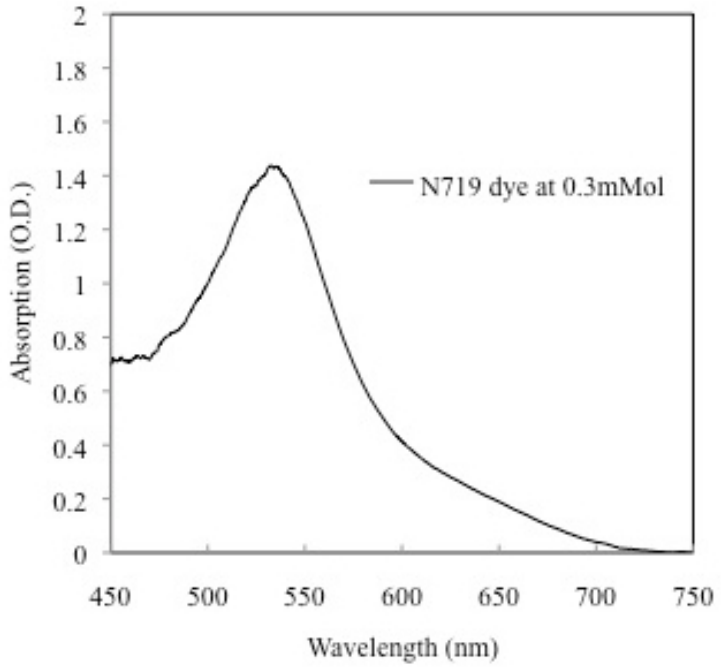

Figure 5.2. Absorption spectrum of N719 dye.

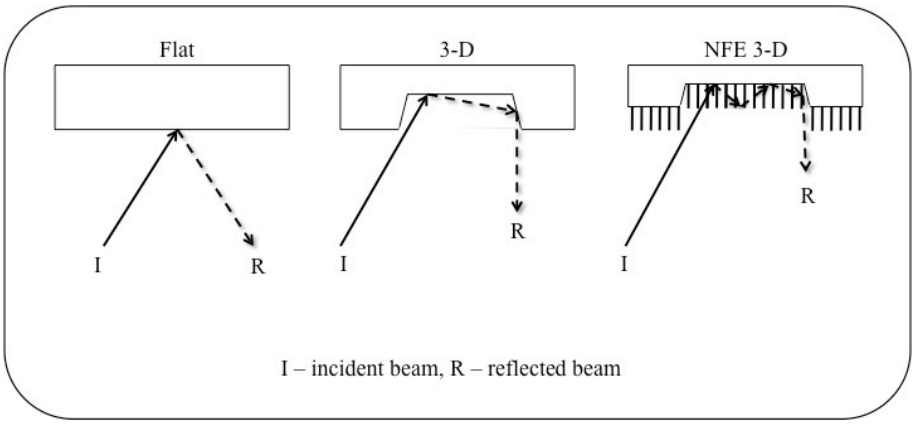

Figure 5.3. Illustration of the effect of surface structure on the optical path of an incident beam.

diagram shows that at incident angles greater than 85 ° to the normal, the light will undergo total internal reflection (TIR). This is the principle that fiber optics is based on which is ideal for light-trapping in photovoltaics. Also, Figure 5.5 shows that less than 1% of the incident power from 0 to 90 ° respect to the normal is reflected. The coating of this nanotube film with N719 dye or any dye for that matter will increase the absorption of the incident beams. It is expected

that increase photon retention can be observed by the reduction of surface reflectance. The reflectance measurements were taken at a 45° angle of incidence.

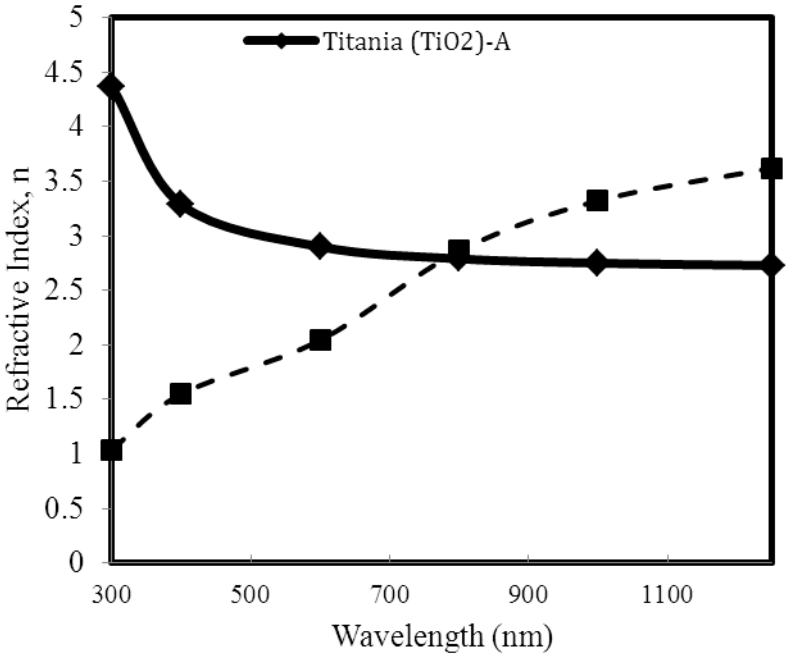

Material	***300 nm***	***400 nm***	***600 nm***	***800 nm***	***1000 nm***	***1250 nm***
Titania (TiO_2)-A	4.372	3.286	2.9	2.79	2.75	2.728

Figure 5.4. Wavelength dependent index of refraction for titania and titanium [4].

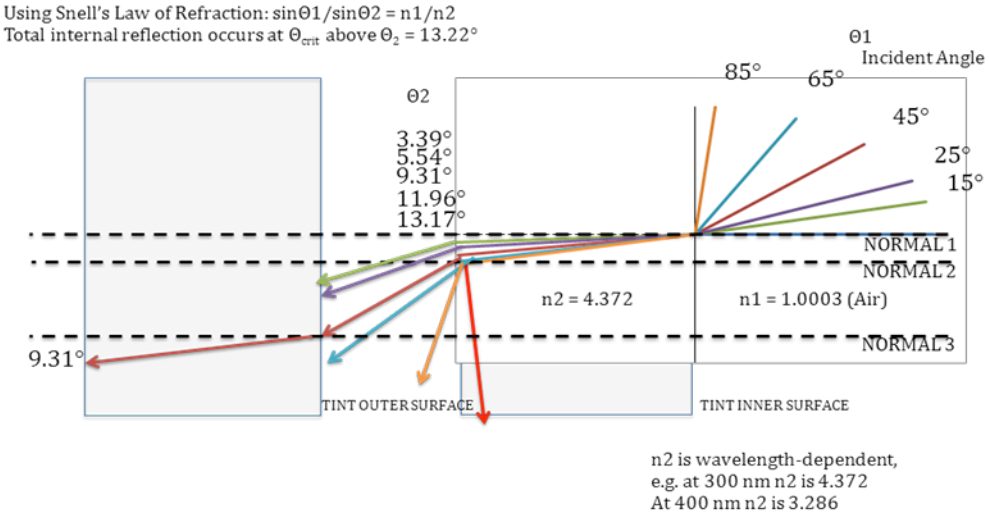

Figure 5.5. Light interaction behavior of various incident angles of light onto outer and inner titania nanotube walls. The illustration is shown for 300 nm.

The source used for all optical measurements was a Halogen lamp. The reference used was a gold-coated silicon wafer.

5.2.5 Photo-Current Density (J-V) Measurements of the NFE Photoanode

In the formation of the solar cell, metal-semiconductor and semiconductor-semiconductor interfaces or junctions are formed. As discussed in Section 1.2.1, each material has a work function or energy level associated with it. When the junction of the two dissimilar metals is made, energy equilibrium (E_F) is met. This equilibrium is through the movement of charge carriers over the junction until there is a charge balance. When a negative charge carrier (e^-) moves from one material to the other, it leaves behind its positive charge carrier counterpart (h^+). At the interface, an energy barrier of e^--h^+ charge carriers is created. Also, in the semiconductor region near this interface, a depletion region is formed in which there are no charge carriers present. The flat energy band diagram for each material is then altered with curvature, indicating that energy equilibrium between the Fermi energy levels of the two materials has been met. At this moment, the joined material now has a built-in internal potential across the newly formed energy barrier. For a charge carrier to move across this energy barrier, it requires external energy from incident light or from a bias voltage.

In the operation and characterization of the solar cell, metal contacts are placed so as to collect the majority charge carriers from the illuminated photovoltaic material. A positive or negative bias voltage can be applied across the cell using these contacts, and current can also be read through these contacts especially in the case of zero bias voltage.

The photo-current-voltage characteristics for N719 dye-sensitized NFE photoanodes only, were measured using Nano Electrical Contact Resistance (NanoECR^{TM}, Hysitron) connected to a Keithley source generator. The principle of NanoECR^{TM} is based on contact

resistance. Figure 5.6a is an image of the measurement apparatus without the chamber housing. Contact resistance is a measurement of the resistance of a material as a whole. Forward current is driven through the sample from the base to the tip. The tip simultaneously measures bias voltage and current drop across the sample. In reference to Figure 5.6b, the layers from bottom to top of the sample are: (1) silver paste, (2) p-type silicon, (3) Ti/TiO_2, and (4) N719 dye

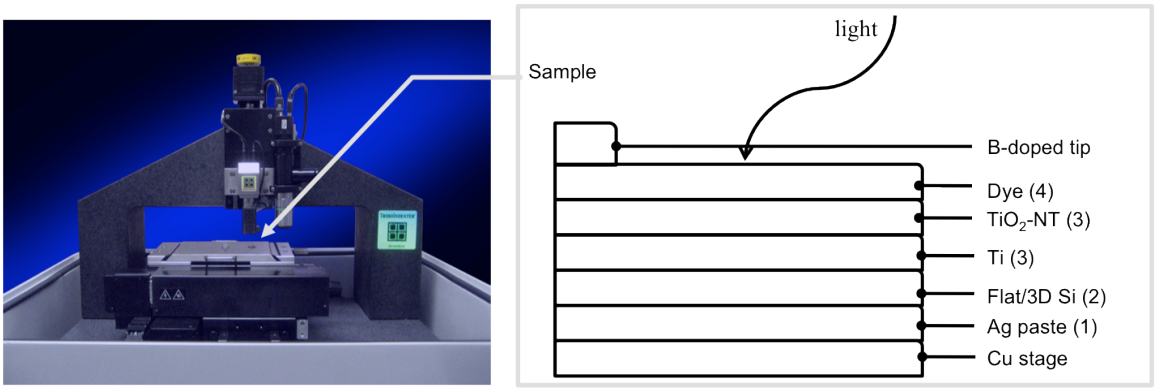

(a) (b)

Figure 5.6. (a) Image of the NanoECR™ measuring apparatus [5], and (b) schematic cross-sectional illustration of the NFE photoanode-only sample measurements.

coating. Bias voltages from -1 to 1 volts were applied and the current was measured via a Boron-doped Berkovich tip. Illumination of the cell was with an array of light-emitting-diodes (LEDs) which was housed within the NanoECR™ chamber. The output power of the LEDs at the sample level

5.2.6 Photo-Current Density Measurements of the NFE DSSC

Photocurrent measurements were taken of a basic assembled DSSC utilizing the NFE 3-D photoanode. Figure 5.7 is an illustration of the cross-sectional view and of the assembled DSSC and Figure 5.8 is of the solar simulation and data acquisition setup. The photoanode was coated with N719 dye and allowed to dry at room temperature for 48 hours. Iodide/triiodide electrolyte was coated onto this. Then ITO glass was placed on top. The cell was held together using

alligator clips as pictured. A Xenon lamp (Oriel) operated at 1000 W/m^2 was used to simulate solar lighting conditions at 1.5AM. The I-V meter was set to measure current while performing a voltage sweep between -1 V to 1 V.

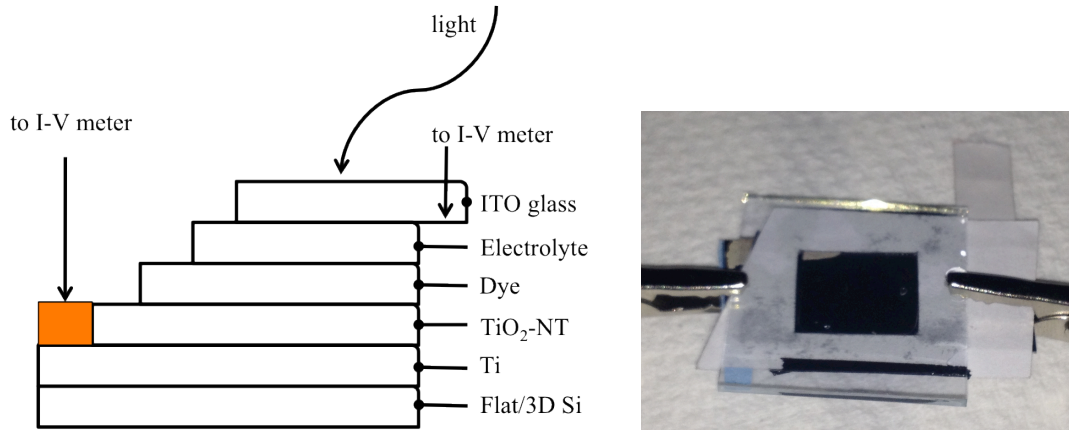

Figure 5.7. Cross-sectional illustration of a complete DSSC. Pictured along side is the actual completed cell.

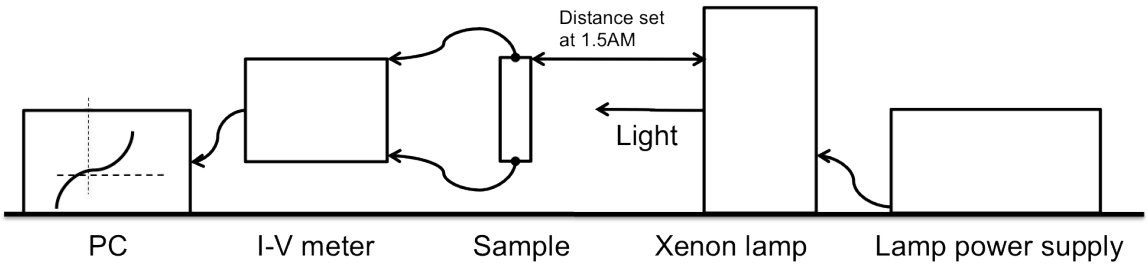

Figure 5.8. Schematic layout of the solar simulation equipment and setup.

5.3 Results and Discussion

5.3.1 X-Ray Diffraction

Figure 5.9 shows the grazing angle X-ray diffraction results. Probing the as-synthesize NFE 3-D surface textured substrate using 1D mode coupled with the Lynxeye detector, Figure 5.9 indicates anatase titania (PDF 89-4921) is the major phase present with the minor phase being that of rutile. The major peaks observed in Figure 5.9 are correlated to the anatase crystal structure having hkl planes 25.33^o 2q - (101), 36.98^o - (103), 37.82^o - (004), 38.60^o - 112, 48.09^o

– (200), and 55.12° – (211) respectively. Figure 5.10 - 2D spectra was probed using the VANTEC-500 2D detector, shows the preferred orientation alone the (004) reflection plane noted by the spottiness of the intense peaks. The (004) peak which is parallel to (001) is observed at 37.82°. The (004) reflection plane is critical to determining the orientation of the as-synthesized anatase titania 3-D surface textured photoanode film. Due to the degree of intensity spottiness observable on the spectra at the (004) reflection hkl plane leads to the conclusions the major phase anatase titania is highly textured. This pronounced texture indicates that a biaxial texture effect in the in-plane orientation of the nanofilm is locked with respect to the 3-D surface textured silicon substrate. This in-plane orientation is aligned along the polar axis (004) reflection hkl plane as related to the silicon substrate orientation but also indicates polycrystalline anatase titania with good morphology and minimum surface defects while yielding a continuous well formed anatase film.

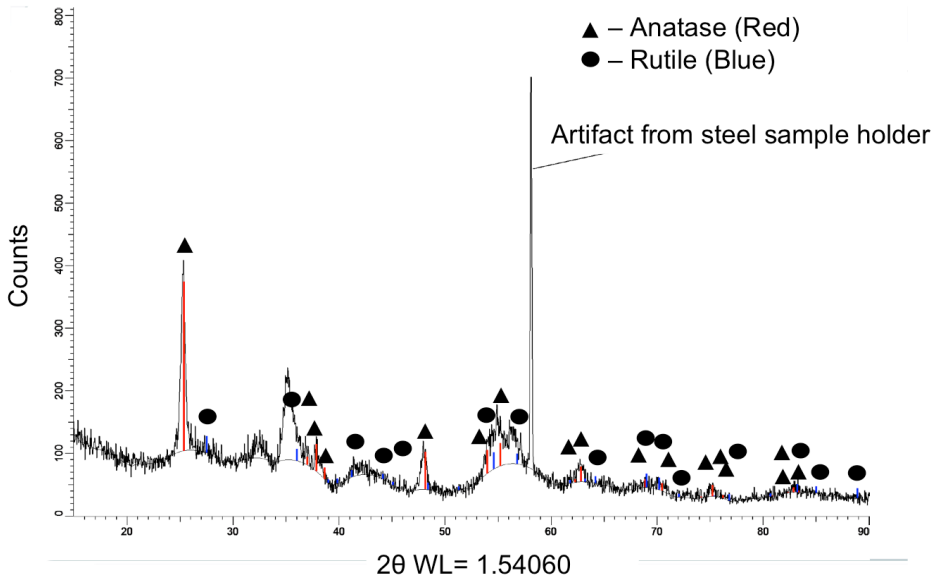

Figure 5.9. Grazing angle x-ray diffraction of NFE 3-D photoanode. Data provided by Bruker.

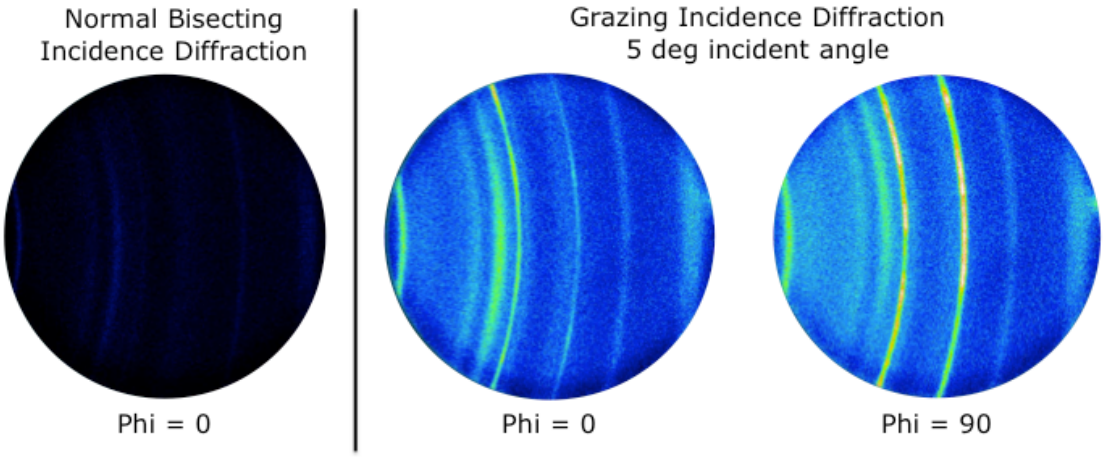

Figure 5.10. Grazing-angle diffraction indicating the presence of 3-D surface texturing. Data provided by Bruker.

5.3.2 Spectral Reflection

Figure 5.11 shows the spectral reflection of the dye-loaded NFE 3-D photoanode. As the surface structure of the photoanode is enhanced, the reflectance of incident photons is reduced meaning more photon energy is retained. At peak wavelengths a 51% reflection reduction is observed for NFE flat to NFE 3-D, and a 78% reflection reduction is observed from dye-sensitized NFE flat to dye-sensitized NFE 3-D photoanode. The peaks for these particular spectra exist due to the color of the anodized nanofilm and the color of the N719 dye.

5.3.3 Dye-Loading Capacity

Figure 5.12 shows the flat versus 3-D dye-loading capacity (solid lines) with the dye molar concentration fingerprint spectra represented as dotted lines as a reference. The small absorption (optical density) difference of 0.1 between flat and 3-D photoanode corresponds to a 5.7 times increase in dye-loading capacity. The SEM image of the dried N719 dye film is shown as an inset. The dye particles are on the sub-nanometer scale and are connected in a web-like formation. The scale bar is 1 micron.

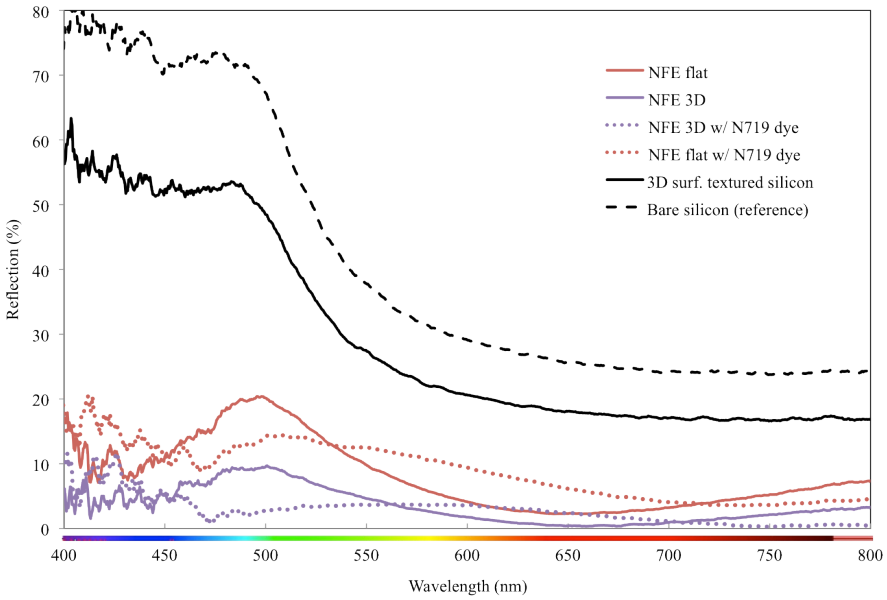

Figure 5.11. Reflection measurements comparing NFE flat to NFE 3-D photoanodes. Bare silicon and 3-D textured silicon are shown as a reference.

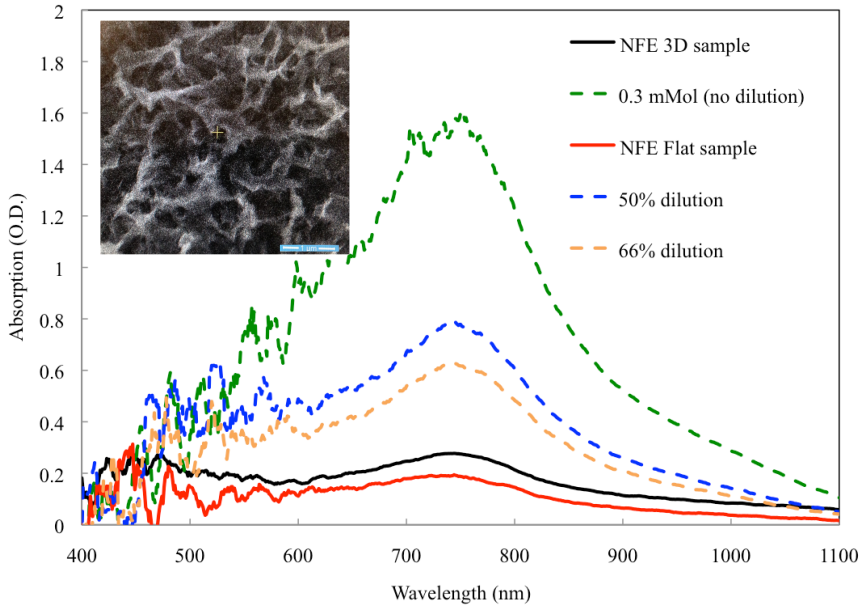

Figure 5.12. Optical absorption changes of diluted N719 dye solution. The inset is an SEM image (scale bar = 1 micron) of the dried N719 dye film on a flat surface.

5.3.4 Photo-Current Density Characteristics of the NFE Photoanodes

Figure 5.13 shows the spectra of the LED array source used for the illumination of the NFE photoanodes with the absorption spectrum of N719 dye. The 5 W/cm^2 LED array light source, although low in power, nearly matches the absorption spectrum of the N719 dye. This

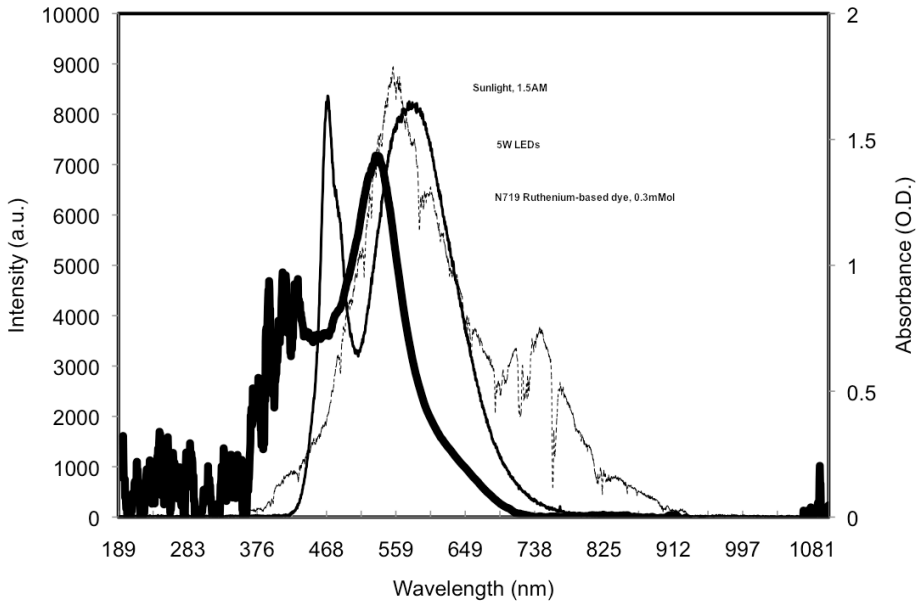

Figure 5.13. Spectrum of the 5 W/cm^2 LED array source used for NFE photoanode illumination shown with respect to the N719 dye absorption spectrum and sunlight at 1.5AM as a reference.

means that nearly the entire energy range of the LED source will be absorbed by the N719 dye giving maximum absorption efficiency. Figure 5.14 shows the forward bias current of the 3-D and flat photoanodes driven by a positive bias voltage in the dark and illuminated. The NFE 3-D photoanode shows a significant increase in forward-bias current density over the NFE flat photoanode. The approximated slope for the NFE 3-D photoanode is 18 whereas the slope for the flat photoanode is 1.7. Therefore, a 5 - 6 times increase in surface area and dye-loading capacity results in an order-of-magnitude increase in forward-bias current density compared to the flat photoanode. Figure 5.15 is a magnified view of Figure 5.14 showing the X- and Y-axis intercepts of the curves. The illuminated NFE 3-D photoanode shows a short-circuit photo-current density of approximately 94 mA. The open-circuit voltage is approximately 18 mV. This shows that with increase in surface area comes an increase in dye-loading surface adsorption and increase in photocatalytic activity per unit surface area giving rise to a higher short-circuit current density. In other words, there is a significant increase in the generation and diffusion of charge-carriers across the internal energy barrier for the high-surface area NFE 3-D

photoanode. The NFE flat photoanodes, however, did not show any significant signs of photoactivity under illumination and behaved more so as a diode. This is not quite understood completely, but may be due to the low power illumination of the LED array source and low-absorption properties of the flat surface.

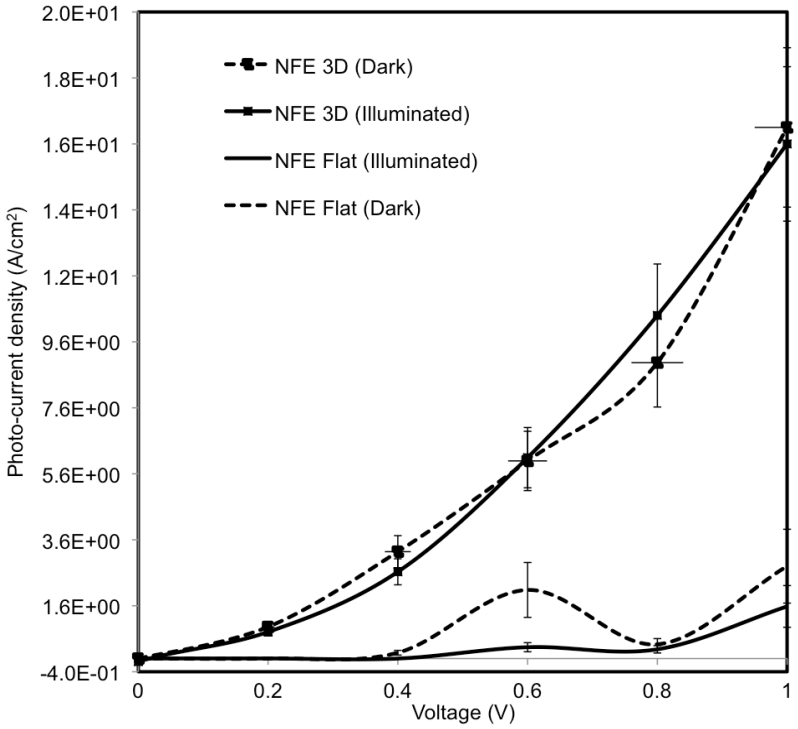

Figure 5.14. Forward bias portion of photo-current density measurements of NFE 3-D and flat dye-sensitized photoanodes illuminated under low power. Standard deviation percentage is 15% for 3-D and 40% for flat samples.

Illumination of the photoanode only with sunlight or solar simulation using the NanoECR^{TM} would have been ideal, however this was not possible given the current setup of the system. Therefore, photoanode-only samples were also measured with the Xenon lamp source solar simulation setup. Figure 5.16 is the forward-bias portion of the photo-current density curve for the photoanode-only under solar simulation. The trend of high-current density for the NFE 3-D photoanode-only sample measured under solar simulation is consistent with the measurements under low-power NanoECR^{TM} measurements. However the scale is not identical. Photo-current

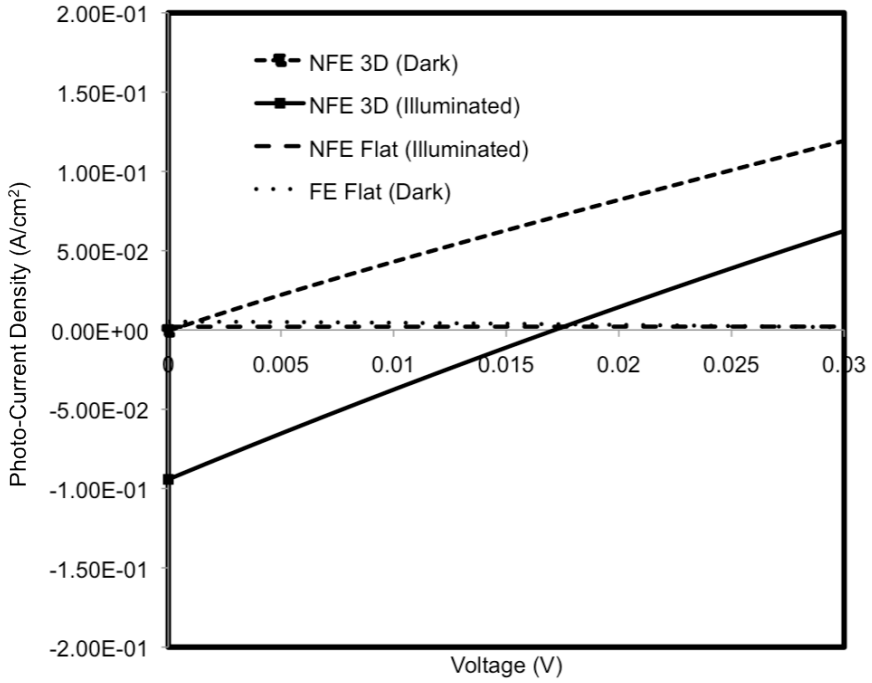

Figure 5.15. Magnified view of J-V curve for the NFE 3-D and flat samples under dark (hashed) conditions and low-power illumination (solid).

measurements with the NanoECR^{TM} result in higher readings on the order of Ampere, whereas the solar simulation measurements result in lower reading in the micro-Ampere range or lower. This difference in scale could be due to the difference in the method of contact between the instruments. Contact with the NanoECR^{TM} is made with a very fine Berkovich tip with nanometer scale surface area. The contact surface area is stable and finely controlled.

Contact surface area using the solar simulation setup is made using alligator clips. The use of these clips does not provide stable and consistent contact surface area. The contact surface area, on the millimeter scale, is also significantly larger resulting in a lower current scale than the nanometer scale tip contact surface area. This instability and measurement inconsistency is shown in Figure 5.17 where both I_{sc} and V_{oc} (Figure 5.17a and Figure 5.17b respectively) cannot be determined with certainty.

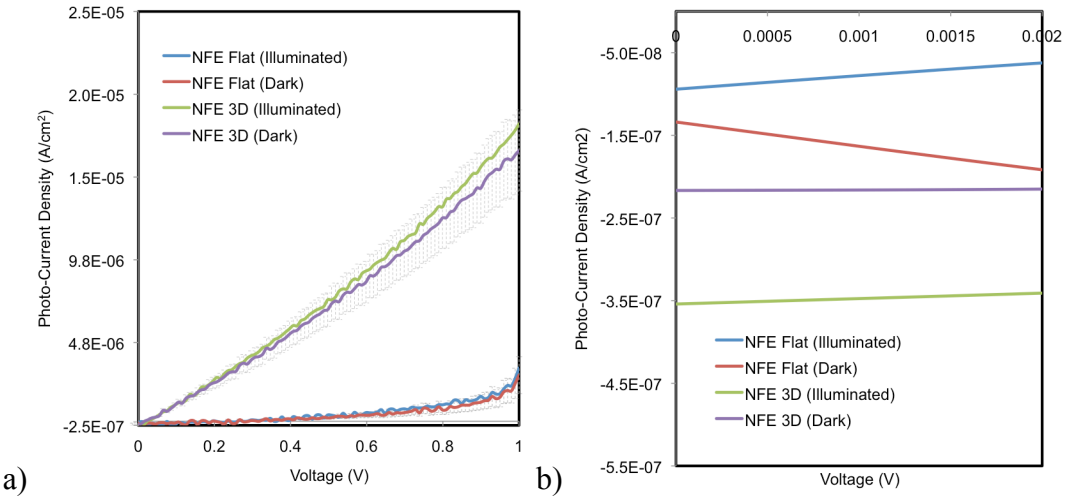

Figure 5.16. (a) Forward-bias portion of the J-V solar simulation measurements of 3-D and flat photoanode-only samples, and (b) Magnified view of J-V curve to show I_{sc} values. Standard deviation percentage is 15% for 3-D and 40% for flat samples.

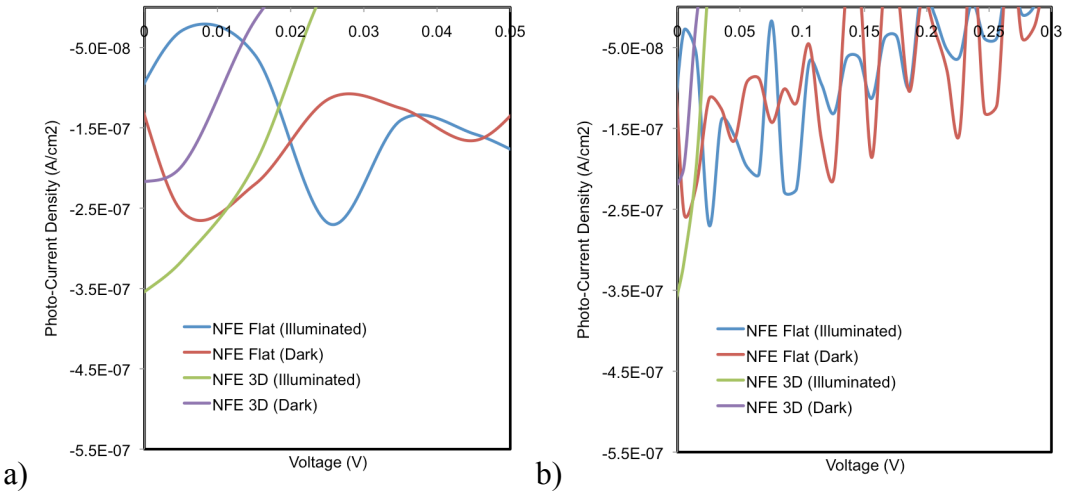

Figure 5.17. (a) Magnified view of the J-V curves showing V_{oc} for the 3-D photoanode-only samples under dark and illuminated conditions and, (b) Magnified view of the J-V curves showing V_{oc} for the flat photoanode-only samples under dark and illuminated conditions.

5.3.5 Photo-Current Density Characteristics of the NFE DSSCs

Figure 5.18 shows the photo-current density measurements (primary axis) of the NFE 3-D and flat photoanodes within a DSSC under forward bias voltage. The current-density measurements of the photoanode-only samples (plotted on the secondary axis) are also shown as a comparative reference. As with the photoanode-only measurements, the high-current density of the NFE 3-D over the low-current density of the NFE flat is maintained. There is a 3 order-of-

magnitude drop however in the forward current density read of the DSSCs compared to that of the photoanode-only. This is most likely due to increased resistance by the electrolyte and ITO glass, and the metal contacts used. Figure 5.19 is a magnified view of the X- (main graph) and Y-intercepts (inset) of Figure 5.18. Open-circuit voltage for the NFE 3-D DSSC is approximately 10 mV, with a short-circuit current density of approximately 0.015 mA.

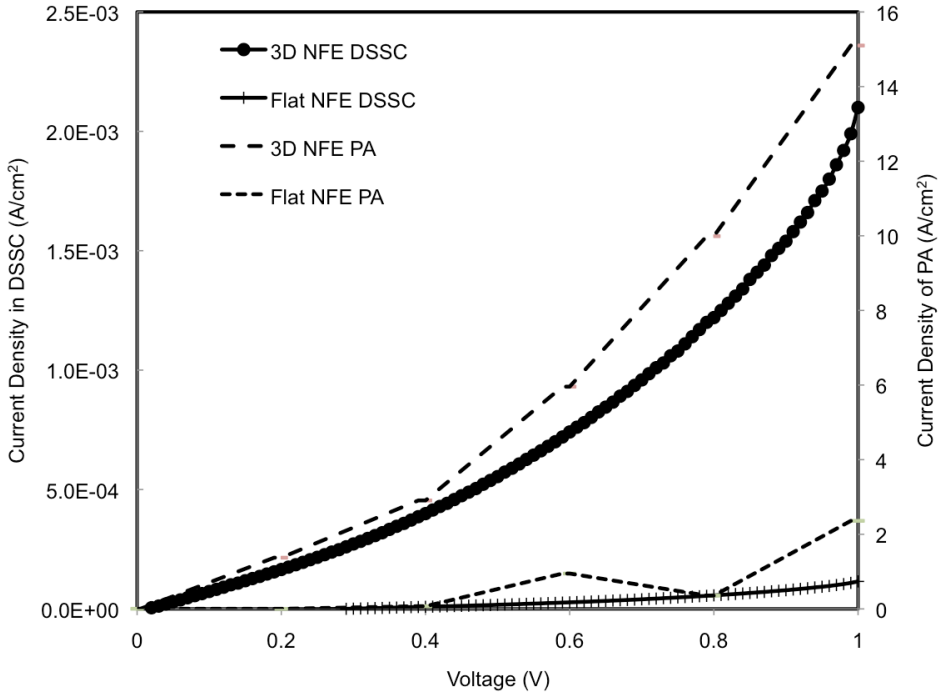

Figure 5.18. J-V curves of NFE Flat vs NFE 3-D photoanode-only (PA) and within DSSC.

The open-circuit voltage of the NFE flat DSSC is 290 mV, with a short-circuit current density of approximately 0.028 mA. It shows that the NFE flat photoanode DSSC is outperforming the NFE 3-D DSSC. Initially this was not expected, however an explanation of this may be seen in the architecture of the constructed DSSC. Figure 5.20 is an illustration showing the NFE 3-D DSSC architecture to the NFE flat DSSC. As noted in the illustration, the non-conforming ITO glass layer introduces large potential pockets of charge recombination sites within the dye and electrolyte layers. Only the surfaces in closer proximity to the ITO coated glass allow

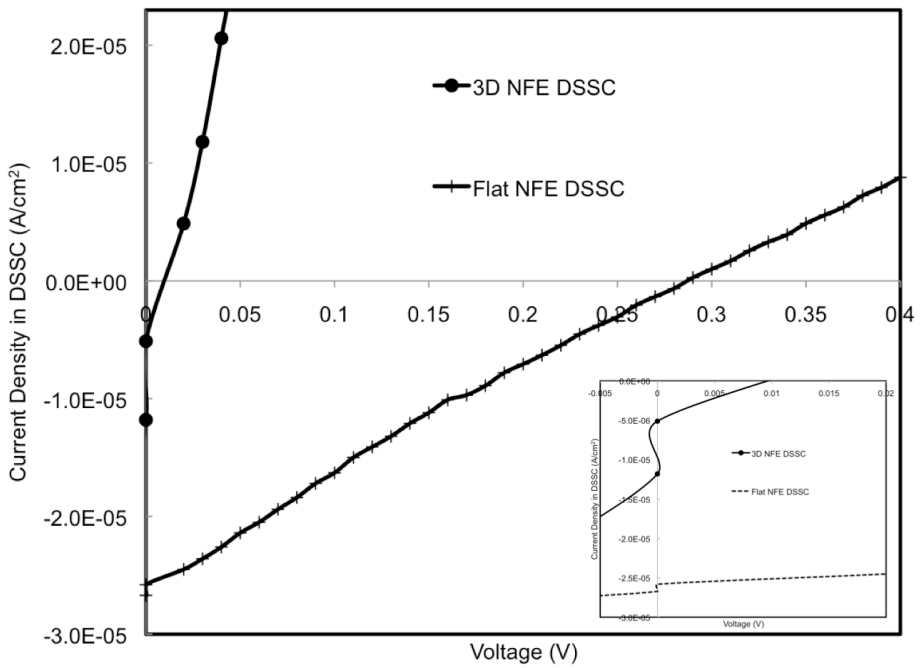

Figure 5.19. Magnified view of photo-current density curves of NFE DSSCs taken under 100 mW/cm^2 solar simulation. The inset shows multiple Y-axis intercepts.

for the collection of moving charges, whereas the additional surface areas provided by the etched silicon planes are not being utilized. The inset shows a peculiar behavior of multiple y-intercepts of each curve. This could be due to some inherent instability within the DSSC construction, and more investigation into this is required.

Degradation of the samples was also investigated. Samples were exposed for the duration of the photo-current tests then placed in the dark, then illuminated again in 1-minute intervals. Figure 5.21 shows an initial photo-current measurement, followed by another exposure after 5 min noted as (a) in the figure. The curves show that the NFE 3-D photoanode DSSC sample begins to degrade rapidly towards the NFE flat photoanode DSSC sample. The expected path of the continued degradation is noted as (b) in the figure.

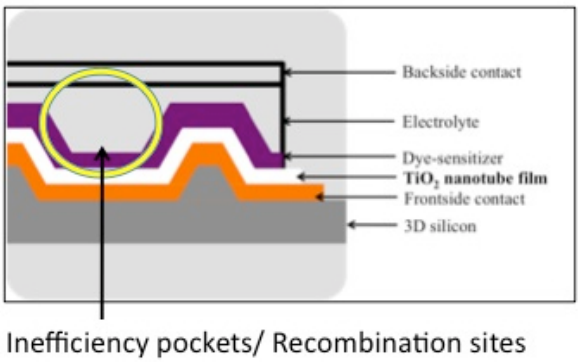

Figure 5.20. Likely explanation for the observed decrease in efficiency of the integrated NFE 3-D photoanode over the flat photoanode.

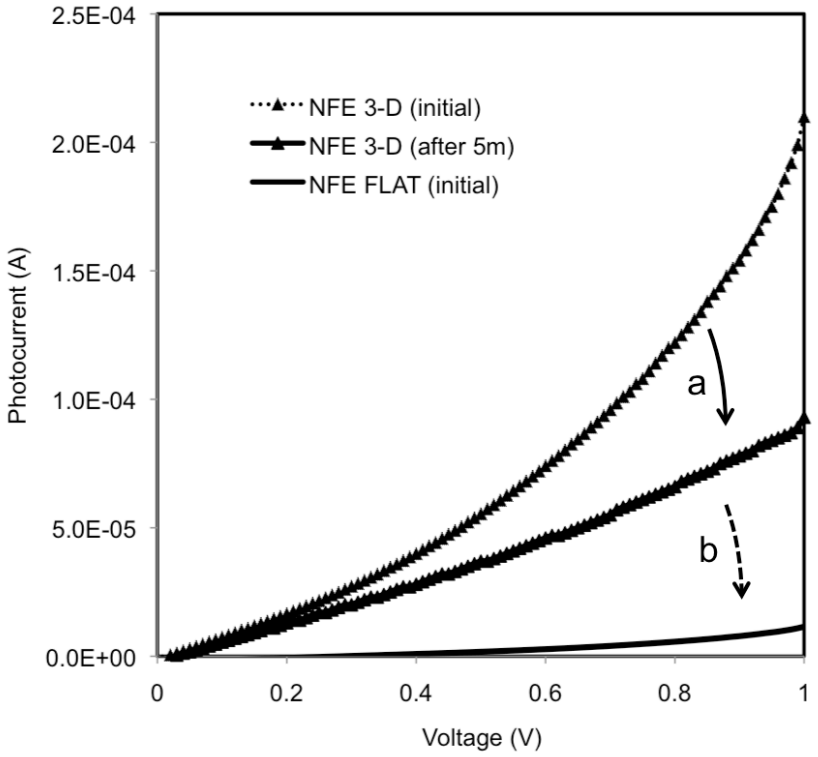

Figure 5.21. Photocurrent curves showing (a) the measured degradation of the NFE 3-D DSSC and (b) the expected path for continued degradation.

5.4 Summary

Dye-sensitized nanotube film enhanced 3-D surface-textured photoanodes were fabricated using MEMS-compatible processing conditions and measured for their adhesive, optical, and electrical properties. The nanotube films exhibited good adhesion on the silicon

surface. Anatase and rutile phase of the titania was present along the 3-D film surface. The NFE photoanode resulted in more than 5 times increase in surface area in comparison to flat photoanodes which increased the dye-loading capacity by a factor of 5. At peak wavelength values, a 78% increase in photon absorption of the dye-sensitized NFE 3-D photoanode was observed. These surface-textured enhancements resulted in an order-of-magnitude increase in forward current-density over NFE flat photoanode-only measurements. The photo-current density measurements of the NFE DSSC samples indicate that a conformal-like coating of the ITO contact layer is required to efficiently utilize the entire NFE 3-D photoanode.

5.5 References

[1] D. A. H. Hanaor, C. C. Sorrell, Review of the Anatase to Rutile Phase Transformation, Journal of Material Science, 2011, 46, 855–874.

[2] www.bruker.com. Accessed on 10/18/13.

[3] M. Bouroushian, T. Kosanovic, Characterization of Thin Films by Low Incidence X-Ray Diffraction, Crystal Structure Theory and Applications, 2012, 1, 35-39.

[4] Indices of refraction values obtained from www.filmetrics.com, www.refractiveindex.info, accessed on 9/2/12.

[5] Image from www.hysitron.com. Accessed on 11/6/13.

CHAPTER 6. INTEGRATION OF NFE PHOTOANODE INTO MICROSYSTEMS

6.1 MEMS/Microsystems

DSSCs have been limited in application largely due to the liquid electrolyte. However, with many efforts and breakthroughs in gel-based, polymer, and solid-state electrolytes, the use and implementation of DSSCs and photoanodes in general is increasing. One of these uses is in providing power to microsystems. It was shown in Chapters 3 and 4, that formation of a nanotube-thin-film-enhanced photoanode onto 3-D silicon microstructures is possible. The microstructures presented were basic, however depending on the purpose, the microstructures can be more complicated. The field of MEMS has been around for many years and with the advent of the Scanning Electron Microscope (SEM) providing the ability to clearly image on the submicron and nanoscale, many structures have been created for various functions. Many of these structures require power. Here is a discussion of some of these structures and their use, and the minimum energy requirements needed for them to operate. We also provide a process to implement NFE 3-D as well as flat photoanodes into these systems either as photoanode-only or as DSSCs to provide an on-board source of power.

6.2 Microsystems Energy Requirements

The current work investigated the current generated within 1 cm^2 area. In the implementation of them in a system for which more power is required, the NFE photoanodes or DSSCs can be arranged within a series to achieve more voltage or series to achieve more current. MEMS encompasses a myriad of structures, some of which are active or passive, and some of which may be both. Examples of some MEMS devices and components are: cantilever beams, in-plane (and out-of-plane) resonant structures, microfluidic channels, gears, waveguides, various pillars, columns, and pores for microfluidic filtration, gyroscopes, motors, and nozzles [1]. It is

important to note that these complex components usually are within a more complex system for which the overall energy for operation is known. Implementation of the NFE photoanode onto microsystems is to make a once passive-only structure, both passive and active.

6.3 NFE 3-D Photoanode Fabrication Process Considerations for Microsystems Integration

Consideration of the process for integration of NFE photoanodes and/or DSSCs into microsystems may be best discussed layer-by-layer. Surface texturing, or the fabrication of a 3-D topology using wet or bulk etching is frequently used in MEMS processing. Surface-texturing is not limited to silicon, and can even be a flexible polymer via molding techniques. Deposition of the photovoltaic material should be conformal-like on all surfaces and exhibit good adhesion. In implementing the photoanode into the microsystem, deposition of the metal interconnect layer(s) at this stage may be ideal. Electrochmeical anodization of say titanium should comprise of electrolyte solutions that are compatible with most metals within the system, and should also be easy to rinse off or remove when necessary. Heat treatment, such as annealing may be required but only feasible on silicon, and not polymers. However, methods such as rapid thermal annealing (RTA) could be utilized for annealing thin films on polymers. Dye-coating of the photoactive layer can be performed using dip/spin-coating techniques. Drying of the film preferably would be at room temperature, for a few days. For the electrolyte, liquid should not be considered due to its instability and leaking issues which are not acceptable in a microsystem. Therfore, solid-state, polymer, and gel-like electrolytes may be suitable. Controlling the thickness and deposition or coverage of the electrolyte is also an advantage over the liquid-based electrolytes. Deposition of the backside metal contact film should provide a conformal coating as to efficiently utilize the enhanced surface area of NFE 3-D photoanodes. Following are two proposed methods for integrating NFE 3-D and flat DSSC into microsystems.

6.3.1 MEMS Integrated Backside Illuminated NFE 3-D Photoanode

Within this work, realization of the NFE 3-D photoanode can be implemented into MEMS as a back-side illuminated DSSC. Figure 6.1 is an illustration of a possible implementation of the TiO_2-NT 3-D silicon microstructured photoanode into a back-side illuminated DSSC. The photoanode is shown to be layered on top of the front-side contact, which can be any highly conductive metal interconnect such as copper or gold and would serve to transfer the photogenerated current to a microsystems or MEMS component. The dye-sensitizer responsible for increasing the photo absorption/catalytic range of TiO_2, such as N719, or Black dye coats the photoanode. Followed is the electrolyte layer, preferably a solid-state or transparent gel electrolyte. The last layer is any electrolyte-compatible transparent electrode. Possible candidates for this back-side contact are fluorine-doped tin oxide (FTO) or graphene. This architecture is what was fabricated and analyzed in Section 5.3.5 with the utilization of the unanodized portion of Ti thin film as the front-side contact, the Ruthenium-based N719 (Di-tetrabutylammonium cis-bis(isothiocyanato)bis(2,2'-bipyridyl-4,4'-dicarboxylato)ruthenium(II)) as the dye-sensitizer, the iodide/triiodide ionic liquid electrolyte 1,2-Dimethyl-3-propylimidazolium bis(trifluoromethylsulfonyl)imide, and indium tin oxide (ITO) coated glass

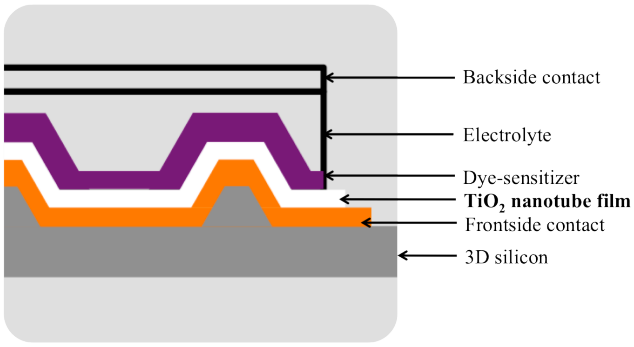

Figure 6.1. Cross-sectional illustration of a backside illuminated NFE 3-D photoanode DSSC for MEMS integration [2].

substrate as the backside contact. As noted in the previous section of considerations, and in Section 5.3.5, the back metal contact must be a conformal coating across the 3-D surface to efficiently utilize the increased surface area.

6.3.2 MEMS Integrated Dual-Side Illuminated NFE Flat and 3-D Photoanode

Implementation of a dual-side illuminated flat photoanode is proposed here. Figure 6.2 is a cross-sectional illustration of this cell based on silicon. Dual-side illumination of a solar cell has the advantage of utilizing incident light from the front-side as well as the back side. For this it is important that the front and back metal contacts are visibly transparent. Patterning of the contacts is most likely not ideal since some areas of the anode would be shadowed from light exposure. Candidates for these metal contacts are ITO, FTO, and graphene. Flexible polymer-based NFE photoanodes also provide a foundation in which to allow dual-side illumination. Figure 6.3 is an image of titanium deposition on a 3-D surface textured PDMS sample. As can be seen, extensive cracking occurs across the deposited surface. This may be due to poor-handling post-deposition. The polymer may also undergo stress during pressure changes in vacuum-assisted deposition. Subsequent steps as discussed in section 6.3 must be compatible and challenges overcome.

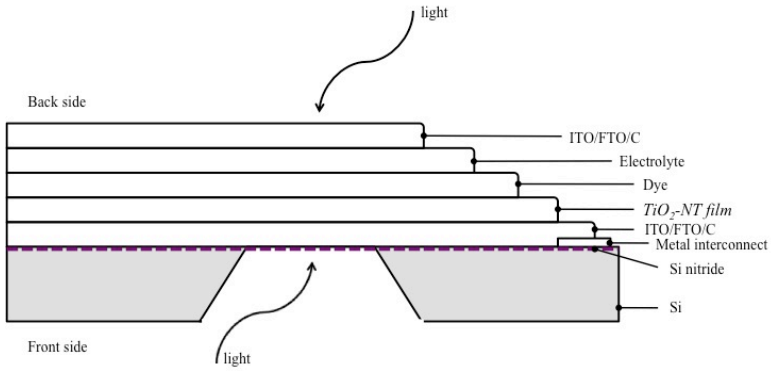

Figure 6.2. Cross-sectional illustration of a dual-side illiuminated Si-based NFE DSSC for MEMS integration.

6.4 References

[1] Gad-el-Hak, M. The MEMS Handbook, CRC, 2002.

[2] F. Dawan, N. Morampudi, Y. Jin, E. Woldesenbet, Hierarchical Fabrication of TiO_2 Nanotubes on 3-D Microstructures for Enhanced Dye-Sensitized Solar Cell Photoanode for Seamless Microsystems Integration. Journal of Microelectronic Engineering, doi: http://dx.doi.org/10.1016/j.mee.2013.10.007.

CHAPTER 7. SUMMARY, CONCLUSIONS, AND FUTURE WORK

7.1 Summary and Conclusions

Dye-sensitized nanotube film enhanced 3-D surface-textured photoanodes were fabricated using MEMS-compatible processing conditions and measured for their adhesive, optical, and electrical properties. The nanotube films exhibited good adhesion on the silicon surface. Anatase and rutile phase of the titania was present along the 3-D film surface. The NFE photoanode resulted in more than 5 times increase in surface area in comparison to flat NFE photoanodes, which increased the dye-loading capacity by a factor of 5. At peak wavelength values, a 78% increase in photon absorption of the dye-sensitized NFE 3-D photoanode was observed. These surface-textured enhancements resulted in an order-of-magnitude increase in current density over NFE flat. The increased performance of NFE 3-D photoanode makes it suitable for use in high-efficiency DSSCs and applicable in the integration of DSSCs into MEMS.

7.2 Future Work

The NFE 3-D photoanode can be viewed as the fundamental layer to achieving higher efficiency in all versions of DSSCs. Packaging the NFE 3-D photoanode in a more efficient DSSC architecture such as conformally coating the back-side contact, utilizing solid/gel-state electrolytes, and using more efficient dye such as Black dye is key to maintaining the high-efficiency of the NFE photoanode and surpassing the current efficiency mark for DSSCs. Furthermore, the formation of thicker and taller nanotubes on high-aspect-ratio microstructures (HARMSTs), and possible surface modification of the TiO_2 nanotubes by doping to increase photocatalytic activity or apparent quantum yield would pave the way for commercialization and widescale use of the photoanodes and DSSCs into MEMS.

APPENDIX A. PERMISSION TO REPRODUCE COPYRIGHTED MATERIAL

The author gratefully acknowledges the permission from the journal of Microelectronic Engineering, Elsevier B.V. for approval to reproduce copyrighted material. The request for copyright use permission is submitted via an online form as shown below.

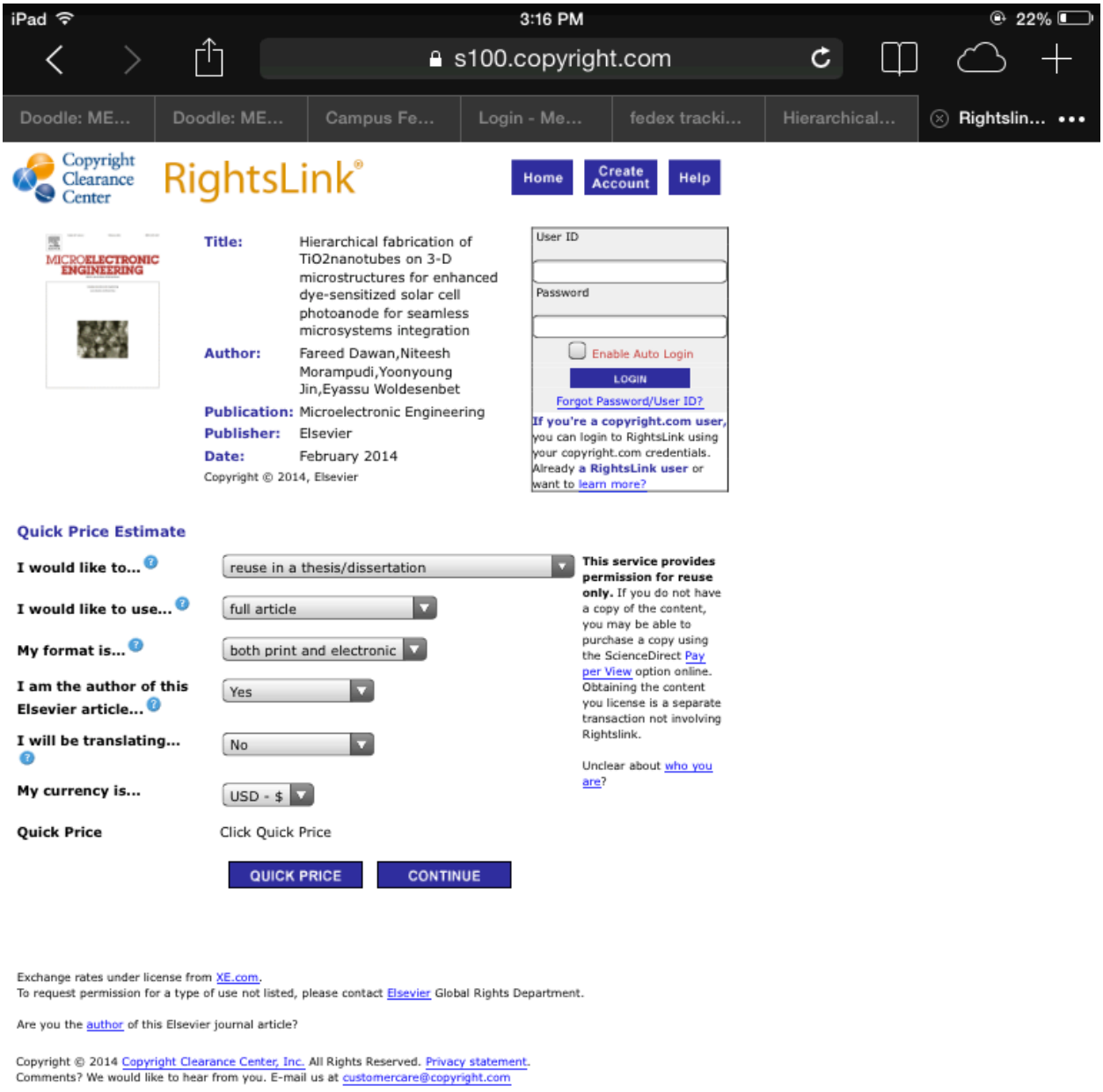

Once submitted, an E-mail is sent verifying the submitted request. Following is the content of this email acknowledging the submitted request followed by the license agreement.

To view this email as a web page, go here.

Do Not Reply Directly to This Email

To ensure that you continue to receive our emails,
please add rightslink@marketing.copyright.com to your address book.

RightsLink | Copyright Clearance Center

Your Request Has Been Submitted

Dear Mr. Fareed Dawan,

Thank you for submitting your request through Copyright Clearance Center's RightsLink service. Elsevier has partnered with RightsLink to license its content online.

Your request will be reviewed within fifteen business days by a member of Elsevier permissions team, after which time you will receive an email with a royalty fee set by Elsevier. **At that time, you must accept the fee and terms to complete the order.**

Please Note: Elsevier may deny your request or you may decline an approved request. In either case, you will receive an e-mail notification. You will not be charged for any request not accepted by you.

Your requested order details are available by clicking the link below:
https://s100.copyright.com/CustomerAdmin/SVP3.jsp?ref=b69d7a33-72e0-4dff-b043-7a81b8d54e76&pName=ELS

Order Details

Licensee:	Fareed B Dawan
Order Date:	Oct 30, 2013
Order Number:	500807298
Publication:	Microelectronic Engineering
Title:	Hierarchical fabrication of TiO2nanotubes on 3-D microstructures for enhanced dye-sensitized solar cell photoanode for seamless microsystems integration
Type of Use:	reuse in a thesis/dissertation
Total:	Not Available

B.3:v6.6

+1-877-622-5543 / Tel: +1-978-646-2777
customercare@copyright.com
http://www.copyright.com

This email was sent to: **fdawan1@lsu.edu**

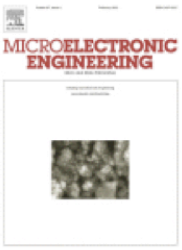

Title: Hierarchical fabrication of TiO2nanotubes on 3-D microstructures for enhanced dye-sensitized solar cell photoanode for seamless microsystems integration

Author: Fareed Dawan,Niteesh Morampudi,Yoonyoung Jin,Eyassu Woldesenbet

Publication: Microelectronic Engineering

Publisher: Elsevier

Date: Oct 22, 2013

Order Completed

Thank you very much for your order.

This is a License Agreement between Fareed B Dawan ("You") and Elsevier ("Elsevier") The license consists of your order details, the terms and conditions provided by Elsevier, and the payment terms and conditions.

License number	Reference confirmation email for license number
License date	Oct 30, 2013
Licensed content publisher	Elsevier
Licensed content publication	Microelectronic Engineering
Licensed content title	Hierarchical fabrication of TiO2nanotubes on 3-D microstructures for enhanced dye-sensitized solar cell photoanode for seamless microsystems integration
Licensed content author	Fareed Dawan,Niteesh Morampudi,Yoonyoung Jin,Eyassu Woldesenbet
Licensed content date	22 October 2013
Number of pages	1
Type of Use	reuse in a thesis/dissertation
Portion	full article
Format	both print and electronic
Are you the author of this Elsevier article?	Yes
Will you be translating?	No
Order reference number	
Title of your thesis/dissertation	Nanotube Film-Enhanced 3-D Photoanode for Application in Microsystems Technology
Expected completion date	Nov 2013
Elsevier VAT number	GB 494 6272 12
Billing Type	Invoice
Billing address	Dept of Mechanical Engineering 2508 Patrick F. Taylor Hall BATON ROUGE, LA 70808 United States
Permissions price	0.00 USD
VAT/Local Sales Tax	0.00 USD
Total	0.00 USD

APPENDIX B. EFFORTS OF SILICON AND 3-D POLYMER METALLIZATION USING E-BEAM EVAPORATION

E-beam deposition of thin metal films is designed to coat thin films of metal on planar surfaces. In order to obtain a conformal-like coating on the non-planar surface, the sample holder was modified. The sample was mounted at an angle of 45 ° with respect to the normal. Rotation of the sample during deposition was performed using the pre-equipped turntable. This setup is shown in Figure 4.1. 100 Å of chromium was deposited onto the samples, followed by 500 Å of gold. The chromium layer serves as an adhesion layer between the SU8 polymer or silicon and gold. Titanium was finally deposited at a thickness of 5000 Å. The quality of the titanium is critical for proper anodization. Two rates at 5 Å/s and 3 Å/s were performed to study the effect deposition rate has on the surface quality of the titanium. The working chamber pressure was 10^{-6} Torr for both depositions.

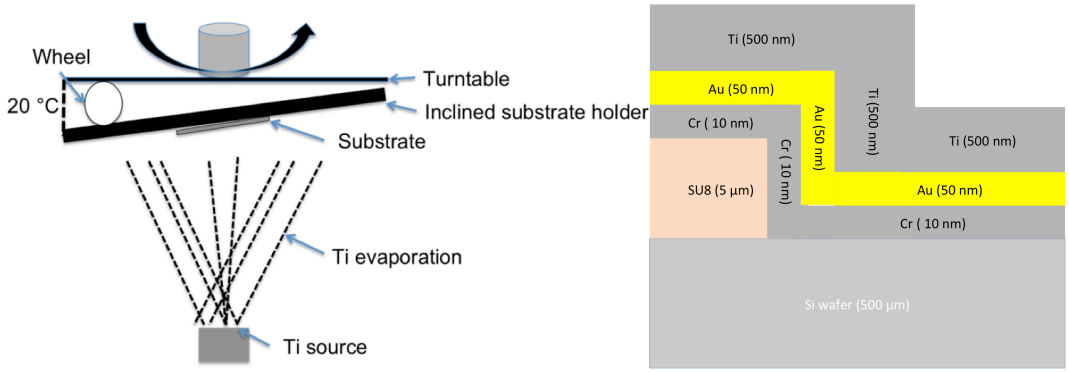

Figure B.1. Setup for inclined deposition of substrates and a cross-sectional illustration of the deposited layers on SU8 polymer and silicon.

Figure B.2 shows a scanning electron microscope image of the deposited film on the 3-D microstructure. The surface of each sample was characterized for its thickness and roughness using the Alpha Step 50 Profiler. Scan parameters were scan length of 500 µm at a scan speed of 5 µm/s. For the tri-metal layer on SU8, an average surface roughness for rates of 5Å/s and 1 Å/s

was 187.9 Å and 338 Å/s respectively. Surface roughness was verified with the Hysitron Nanoindenter TI-9600 in Atomic Force Microscopy (AFM) mode.

Current-voltage (J-V) characteristics were also measured with the TI-9600 Nanoindenter in Nano Electrical Contact Resistance (ECR) mode. For these measurements, a thin layer of conductive silver paste (silver conductive pen, Radio Shack ®) was applied to the bottom of the sample. A simple load function was defined as shown in Figure B.3. Indentations and bias voltages from ±8 V were applied to the sample using a Boron-doped Berkovich tip.

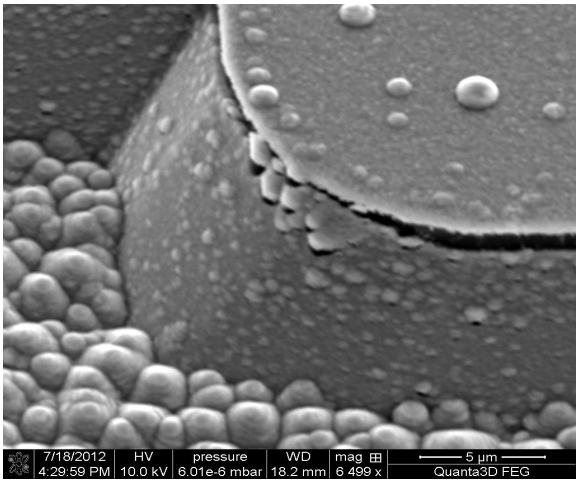

Figure B.2. SEM image of the Ti layer deposition on the 3-D microstructure. Film stress is observed on the edges of the structures.

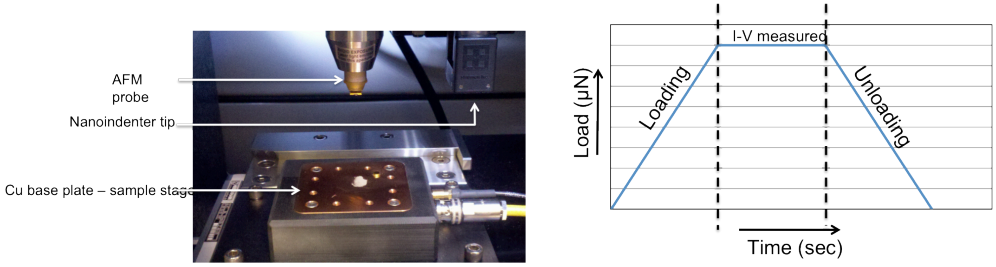

Figure B.3. Nanoindenter NanoECR assembly and loading scheme to measure thin-film J-V characteristics.

Figure B.4 shows current density vs. applied bias voltage for both silicon and SU8. The J-V curves for both surfaces show a non-linear asymmetry. The rectification ratio (forward

current/ reverse current) vs. voltage graph as shown in Figure B.5, confirms this non-linear asymmetry. This J-V profile resembles that for a metal-insulator-metal diode. Determination of whether the tip sinks through the tri-metal layer while undergoing NanoECR testing was performed. Figure B.6 shows this sinking action under a force of 110 and 180 μN for both metal coatings on SU8 and Si at an applied bias voltage of 4 V. From this data, it shows that the tip sinks approximately 40 nm/5 min. This sinking can provide variations from the current reading as the tip starts from the surface into the subsurface and further on into the layers. In order to have consistency throughout all measurements, the current measurements provided are no greater than 5 seconds after applying the voltage. Furthermore, due to the change in measured sample thickness or area from the sinking, J-V characteristics, which are usually used for the characterizing a device, are provided and not J-E, which are used for material characterization.

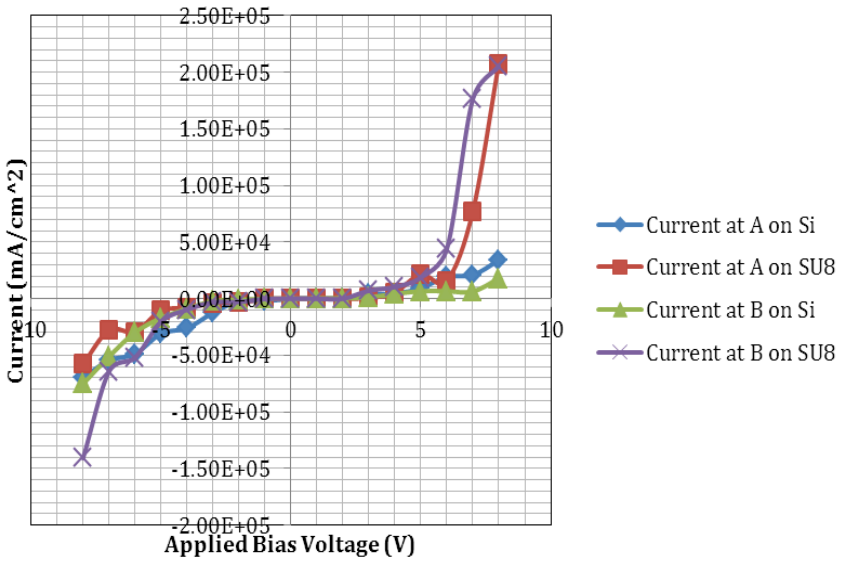

Figure B.4. Graph showing the J-V characteristics of Ti on SU8 (purple and red) and Si (blue and green).

Figure B.7 shows the change in hardness and elastic modulus of the SU8 polymer as the tip sinks. This may be evidence that the SU8 polymer is not fully cured throughout. Therefore, prior to thin-film deposition, steps (such as monitoring solvent bake-out and polymer hardness) must be taken to ensure the polymer is fully cured.

(a)

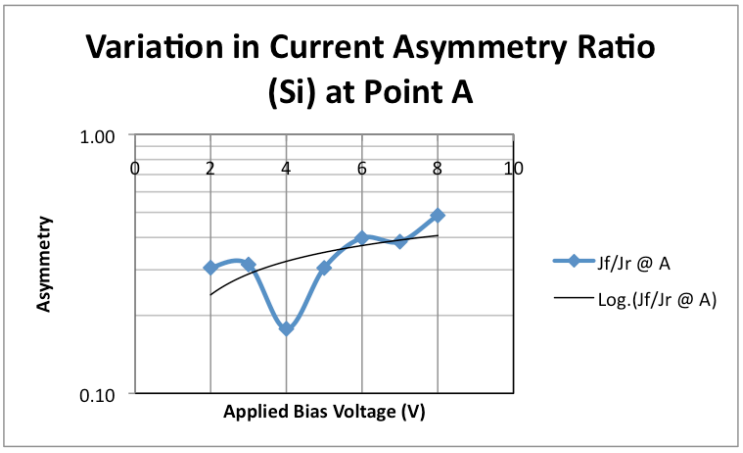

(b)

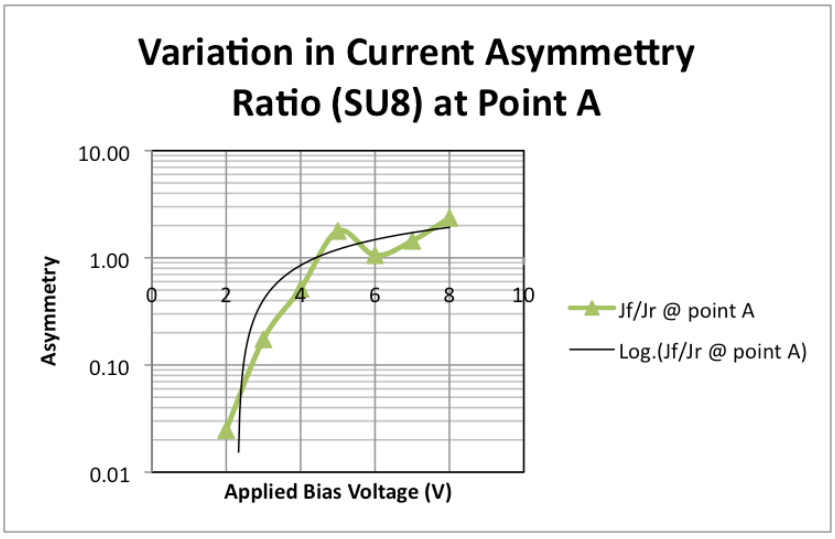

Figure B.5. Variation in current asymmetry ratio for Ti on (a) silicon and (b) SU8 confirming non-linearity of the J-V characteristics for the metal-on-polymer configuration.

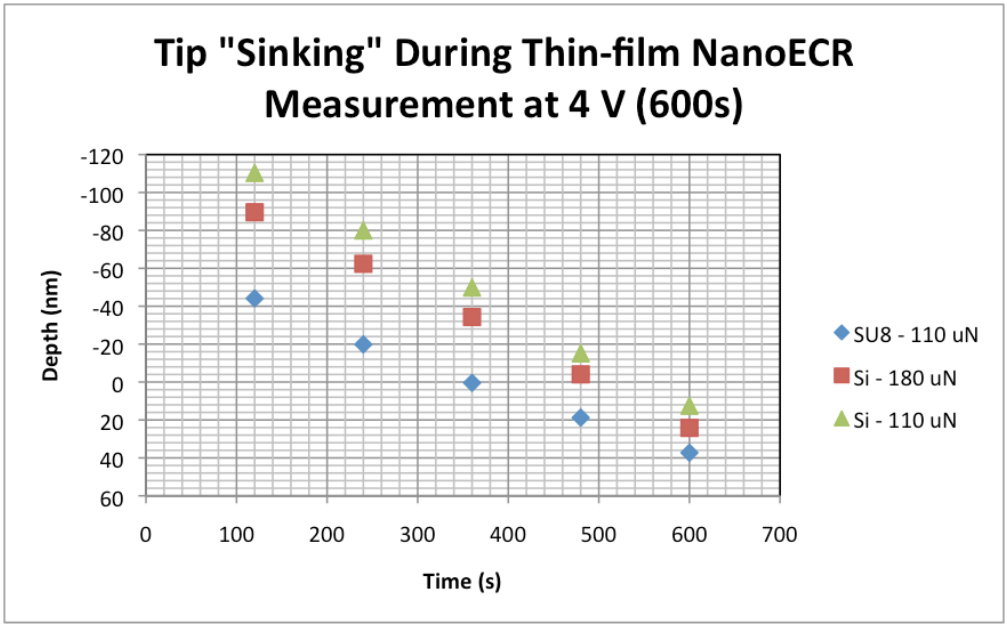

Figure B.6. Graph showing the nanoindentation tip sinking during I-V measurements. The tip sunk about 40 nm within 5 minutes of measuring.

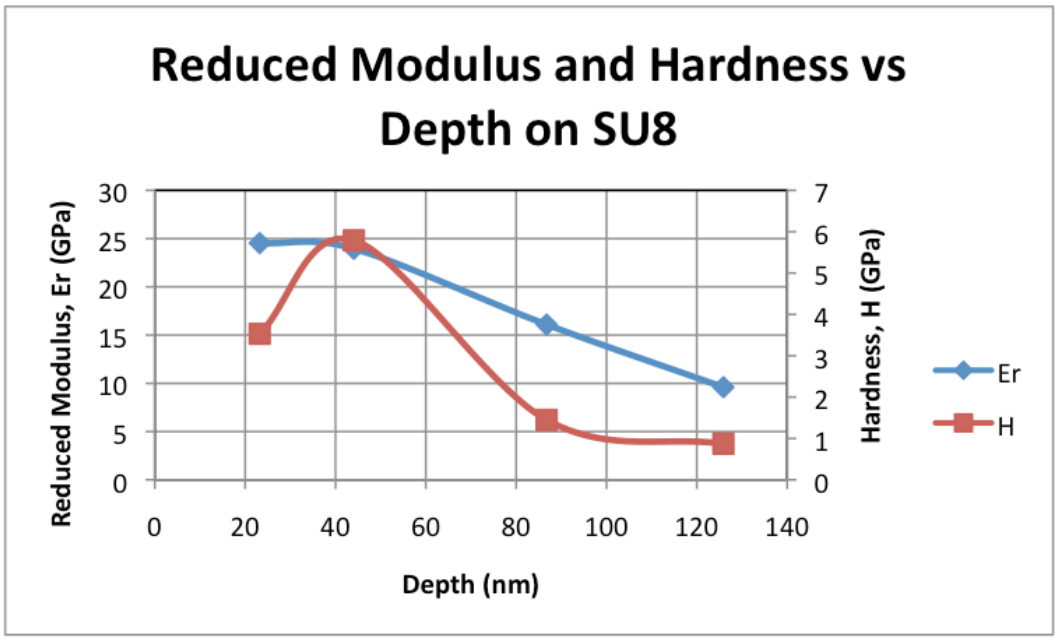

Figure B.7. Graph showing the change in elastic modulus and hardness as the nanoindentation tip sinks during NanoECR measurements.

APPENDIX C. EFFORTS ON THE FORMATION OF TIO_2 NANOTUBES WITHIN E-BEAM EVAPORATED THIN-FILMS ON SILICON AND SU8

Preliminary study of anodization of as-deposited titanium film on planar silicon and SU8 polymer surfaces resulted in TiO_2 nanotubes in 2-micron thick films deposited at a deposition rate of 5Å/s. It has also been found that fully cured PMMA and SU8 are compatible with the anodization electrochemical process.

Titanium foils with a thickness of 30-microns and as-deposited titanium thin-films were anodized using a two-electrode electrochemical system. The cathode was a 2-inch diameter platinum disc with the anode being a 1 cm x 2 cm deposited titanium sample. The electrolyte used is an organic, composed of ethylene glycol, sodium fluoride, and water. The solution was stirred for 15 minutes before use. Anodization parameters for the samples were a potential of 60 V for a duration of 5 minutes.

Figure C.1 is a comparison of SEM images taken of anodized titanium foil and as-deposited thin-film at different times. It is shown that the surfaces of the two differ significantly. This is likely due to the polished surface the Ti foil has whereas the deposited Ti film is amorphous. The foil resulted in nanotubes as seen clearly in Figure C.1 (top right). The as-deposited anodized Ti on SU8 and silicon revealed nanopores on the surface as shown in Figure C.2. When this sample was cut, nanotubes were revealed under the nanoporous surface as shown in Figure C.3. The nanotubes were 0.5-microns tall and about 250 nm in diameter.

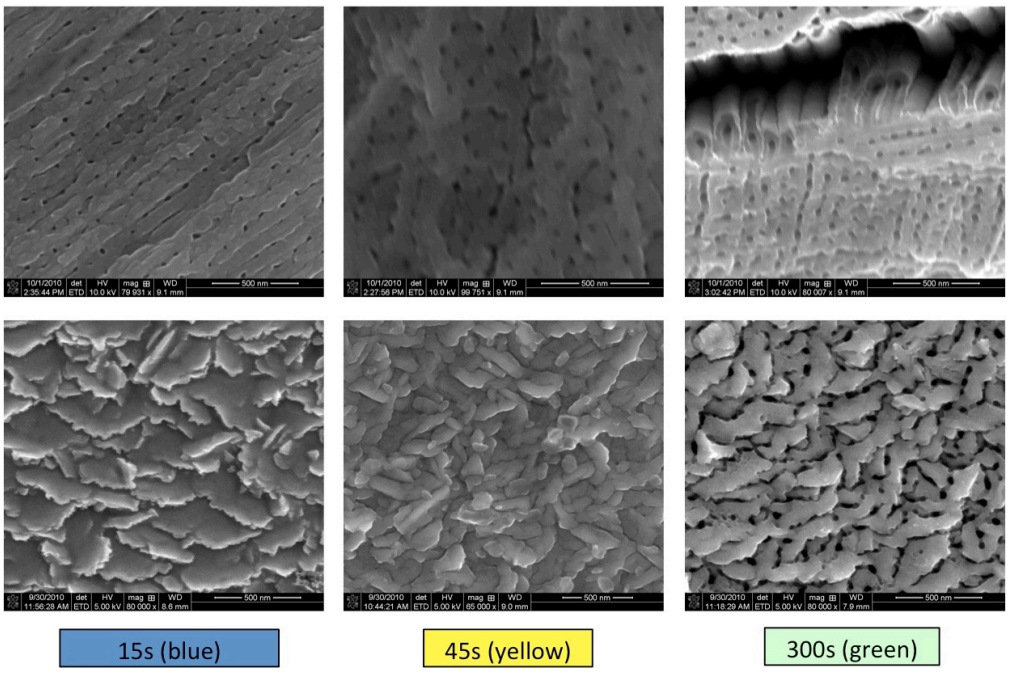

Figure C.1. Surface comparison of anodized titanium foil (top) and film (bottom) at 60V for 15s, 45s, and 300s. The colors given are the actual colors reflected from the samples surface.

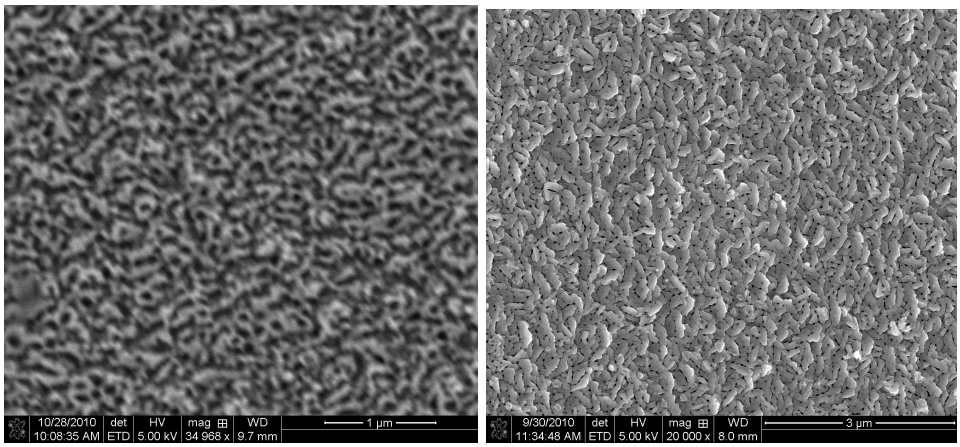

Figure C.2. Surface images showing anodized Ti on SU8 (left) and Si (right).

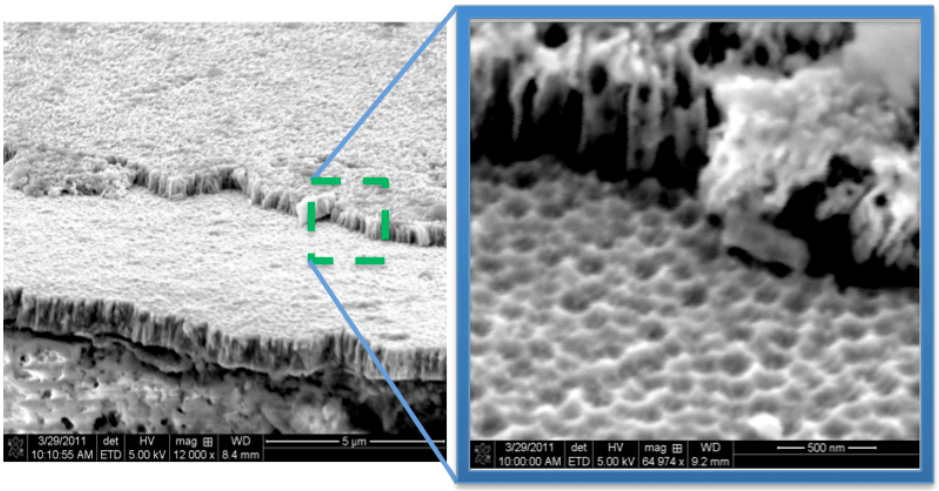

Figure C.3. Titania nanotubes evident from a cross-section of anodized as-deposited titanium on silicon.

A preliminary study on the anodization of as-deposited titanium films on an etched silicon 3-D surface resulted in debonding of the film from the etched plane as shown in Figure C.4. No nanotubes were observed on the debonded film.

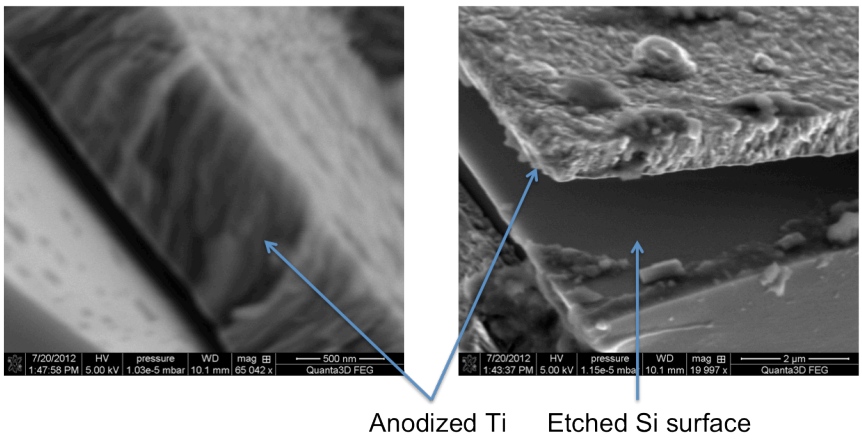

Figure C.4. Debonding of anodized as-deposited titanium film on etched silicon surface.

VITA

Fareed Barakat Dawan was born in Baton Rouge, Louisiana. He received his Master of Engineering degree in The Department of Mechanical Engineering at Southern University in 2006. His thesis research investigated the use of polymer nanocomposites for use as high-functionality MEMS components. He has over 10 years working experience in the area of advanced micro- and nano-fabrication including UV and X-ray mask fabrication and lithography, and vacuum-assisted thin-film deposition. He has extensive experience in materials research and has been published in well-known journals including the Journal of Microelectronic Engineering, the Journal of Microsystems Technologies, and the Journal of the American Chemical Society. Mr. Dawan has also presented his research worldwide at national and international conferences. He is currently serving as both the Administrative Assistant Director and as a Research Associate for the National Science Foundation (NSF) funded NextGenC^3 Composites CREST Center at Southern University.